Exocyst Dynamics During Vesicle Tethering and Fusion

Syed Mukhtar Ahmed[1‡], Hisayo Nishida-Fukuda[1,2,3‡], Yuchong Li[4,5], W. Hayes McDonald[6], Claudiu Gradinaru[4,5] and Ian G. Macara[1*]

[1]Department of Cell and Developmental Biology, Vanderbilt University School of Medicine, Nashville TN 37240 USA
[2]Department of Biochemistry and Molecular Genetics, Ehime University, Japan
[3]Department of Hepato-Biliary-Pancreatic and Breast Surgery, Ehime University, Japan
[4]Department of Physics, University of Toronto, Toronto, ON, M5S 1A7, Canada
[5]Department of Chemical & Physical Sciences, University of Toronto Mississauga, Mississauga, ON, L5L 1C6, Canada
[6]Department of Biochemistry, Vanderbilt University School of Medicine, Nashville, TN 37240, USA

[‡]Equal contributions.

*Corresponding author.

Address correspondence to:

Ian Macara, Ph.D.
Louise B. McGavock Professor, and Chair
Dept. of Cell and Developmental Biology
Vanderbilt University School of Medicine
PMB 407935
U 3209 MRB III
Nashville TN 37240-7935
USA

Tel: 615-875-5565
Email: ian.g.macara@vanderbilt.edu

Character counts:

SUMMARY

The exocyst is an octameric protein complex that is conserved throughout the Eukaryotes and is essential for life. It tethers exocytic vesicles to the plasma membrane prior to fusion. Exocyst assembly and delivery mechanisms remain unclear, especially in mammalian cells. To address these issues we tagged endogenous exocyst subunits with sfGFP or Halo using Cas9 gene editing, to create single and double knock-in lines of NMuMG mammary epithelial cells and used high speed imaging to capture the dynamics of exocyst assembly and disassembly. Surprisingly, we find that as in yeast the mammalian exocyst is comprised of 2 subcomplexes, but these can each associate independently with the plasma membrane and are in a dynamic equilibrium. Moreover, although all subunits arrive at a vesicle fusion site at similar times (~14 sec prior to fusion), departure of one subunit, Sec3, occurs ~1 sec prior to fusion, whereas all others depart just after fusion. Single molecule counting indicates ~9 exocyst complexes associated with each vesicle. These data reveal the mammalian exocyst to be an unexpectedly dynamic two-part complex, and we propose a new model for its assembly and disassembly.

Key words: vesicles, membrane fusion, dynamics, TIRFM, CRISPR, gene-editing, protein complex.

INTRODUCTION

Traffic between membrane-bound compartments requires the docking of cargo vesicles at target membranes, and their subsequent fusion through the interactions of SNARE proteins. The capture and fusion of vesicles are both promoted by molecular tethers known as multisubunit tethering complexes (MTC) (Dubuke and Munson, 2016). One group of such tethers, sometimes called CATCHR (complexes associate with tethering containing helical rods) comprises multi-subunit complexes required for fusion in the secretory pathway, and includes COG, Dsl1p, GARP and the exocyst (Brunet and Sacher, 2014). The endolysosomal pathway contains two different tethering complexes, CORVET and HOPS, with similar overall structures to the CATCHR group (Chou et al., 2016).

COG consists of two subcomplexes, each containing four subunits, which function together within the Golgi (Fotso et al., 2005; Ungar et al., 2005; Willett et al., 2013). The exocyst is also octameric, and is necessary for exocytic vesicle fusion to the plasma membrane, but the organization of the complex has been controversial (Guo et al., 1999; Heider and Munson, 2012; TerBush et al., 1996; Wu and Guo, 2015). Several studies in yeast suggest that one (Sec3) or two (Sec3 and Exo70) subunits associate with the plasma membrane and recruit a vesicle-bound subcomplex of the other subunits, but other work argues that the exocyst consists of 2 subcomplexes of 4 subunits each that form a stable octamer or, in mammalian cells, that 5 subunits at the plasma membrane recruit 3 other subunits on the vesicle (Baek et al., 2010; Boyd et al., 2004; Donovan and Bretscher, 2012, 2015; He et al., 2007; Heider et al., 2016; Liu et al., 2018; Liu and Novick, 2014; Luo et al., 2014; Moskalenko et al., 2003; Yakir-Tamang and Gerst, 2009; Zhang et al., 2008). Rab GTPases promote exocyst binding to the vesicle, and SNARES, Rho family GTPases, the PAR3 polarity protein, and phospho-inositide binding domains are all involved in recruiting exocyst to the plasma membrane (Adamo et al., 1999; Ahmed and Macara, 2017; Das and Guo, 2011; Donovan and Bretscher, 2012; Guo et al., 2001; Pathak et al., 2012; Wu et al., 2010; Yamashita et al., 2010; Zhang et al., 2001). However, the dynamics and regulation of assembly and disassembly of these tethering complexes have not been fully resolved. Indeed, remarkably little is known about exocyst dynamics, especially in mammalian cells. Overexpression of individual exocyst subunits results in aggregation and degradation (Rivera-

Molina and Toomre, 2013). Rivera-Molina and Toomre avoided this problem by silencing the Sec8 subunit and replacing it with low-level expression of a Sec8-RFP fusion protein. Using this approach with total internal reflection (TIRF) microscopy they tracked Sec8 arrival at the plasma membrane, which occurred simultaneously with vesicles about 7.5 sec prior to vesicle fusion and subsequent disappearance of the Sec8-RFP fluorescence (Rivera-Molina and Toomre, 2013). The behavior of other exocyst subunits was not addressed. In budding yeast, vesicles remain tethered for about 18 sec prior to fusion, and several tagged exocyst subunits were shown to dissociate at the time of fusion, suggesting that the complex does not dissociate (Donovan and Bretscher, 2015). However, the time resolution was only ~1 sec, so rapid dynamics could not be tracked.

The advent of CRISPR/Cas9-mediated gene editing coupled with the development of high efficiency scientific CMOS (sCMOS) cameras has the potential to revolutionize our understanding of protein dynamics in the living cell. As proof of principle we have generated multiple tagged alleles of exocyst subunits by gene editing, and coupled proteomics with imaging of the endogenous subunits using high-speed two-color TIRF microscopy, and by fluorescence cross-correlation spectroscopy (FCCS). In conjunction with vesicle fusion markers (pHuji or pHluorin) we discovered that, in NMuMG mammary epithelial cells, exocyst connectivity is different from previous models of the mammalian exocyst but is similar to the recently reported connectivity in budding yeast, with two subcomplexes (Heider et al., 2016). Unexpectedly, however, each can associate with the plasma membrane independently of the other. Subunit arrival at the plasma membrane coincides with vesicle arrival but with an arrival delay between subcomplexes of ~ 80 msec. One subunit, Sec3, which is part of Subcomplex 1 (SC1), departs prior to fusion and the departure of other sub

units. Sec3 also exhibits anomalous diffusion. Fewer Sec3 molecules are present per vesicle than for other subunits, and cross-correlation to other subunits is significantly lower. Taken together, these data are inconsistent with previous models of exocyst function and suggest that, in mammalian cells, intact subcomplexes assemble on secretory vesicles as they dock, and that Sec3 is released prior to fusion. We speculate that this release is important for SNARE mediated fusion.

RESULTS

Generation and validation of functional, endogenously tagged exocyst subunits

Each of the 8 exocyst subunits can be C-terminally tagged in *S. cerevisiae* without disrupting function (Heider et al., 2016). Therefore, we attempted to incorporate C-terminal tags into all exocyst subunit genes of the NMuMG murine mammary epithelial cell line, using Cas9-mediated gene editing. Targeting vectors included superfolder (sf) GFP, mScarlet-i (Sc), or Halo tags, with 1kb 5' and 3' homology arms designed to remove the PAM sequence and the nearby stop codon, and to insert the tag in the correct reading frame (Figures 1A, S1A). Successfully gene-edited cells were isolated by FACS, and single colonies of cells were expanded and genotyped (Figures 1B, S1B-H). GFP+ cell lines were recovered with 5 of the 8 targeting vectors (Figure 1C). For the other subunits, either no GFP+ cells were detected (Exo84), or rare single GFP+ cells were detectable after transfection (Figure S1I, J) but did not proliferate (Sec10, Sec15). Tagging these subunits at the N-terminus was also unsuccessful. NMuMG cells are unusually sensitive to defects in membrane protein delivery, as is caused for example by silencing of exocyst subunit expression, and they rapidly apoptose (Ahmed and Macara, 2017; Friedrich et al., 1997; Hutagalung et al., 2009; Murthy et al., 2005; Roumanie et al., 2005; Wu et al., 2010; Zhang et al., 2008). Therefore, we conclude that tagging Sec10, Sec15 or Exo84 disrupts exocyst function, while C-terminal tags on the other 5 subunits (Exo70, Sec3, Sec5, Sec6, and Sec8) are well tolerated. Homozygous clones of Exo70-GFP, Sec5-GFP, and Sec8-GFP were isolated, plus heterozygous clones of Sec3-GFP and Sec6-GFP (Figure 1C, S1B-E, S1G). We also created a homozygous double knock-in cell line of Sec5-Sc + Exo70-GFP (Figure S1H).

Low but significant GFP fluorescence above the autofluorescence background was detectable by confocal microscopy of live cells for each of the 5 single knock-in lines (Figure 1D). Sec5, Sec6, Sec8 and Exo70 were enriched at intercellular junctions, consistent with data on fixed and immunostained epithelial cells, but the knock-in cells also have substantial diffuse cytoplasmic pools, and no detectable nuclear signal, contrary to some other reports (Torres et al., 2015). Sec3 was anomalous in showing a predominantly cytoplasmic distribution with no significant accumulation at junctions.

To further validate the functionality of the tagged exocyst subunits we performed immunoprecipitations from Exo70-GFP, Sec3-GFP and Sec5-GFP cell lysates using GFP-trap beads, and analyzed them by mass spectrometry. Each tagged protein not only co-precipitated each of the other 7 subunits (Figure 1E, Table S1) but also known regulatory factors (RalA and RalB), RhoGEFs, and proteins associated with intercellular junctions (Balakireva et al., 2006; Chen et al., 2011; Moskalenko et al., 2003; Pathak et al., 2012; Yeaman et al., 2004). We also identified several peptides from a Sec15-like gene, Sec15L. However, no peptides from 4 Sec6-related genes were detected, suggesting that these isoforms are not expressed in NMuMG cells.

In a second approach, immunoblots from the Sec5-GFP and Exo70-GFP precipitations identified co-precipitated Sec8 (Figure S1K). Interestingly, we also identified the SNARE associated protein SNAP23 with Exo70-GFP by co-precipitation and immunoblot as well as by mass spectrometry (Figure S1K, Table S1). SNAP23 was not detected with Sec5-GFP, however, suggesting that SNAP23 is likely not associated with the entire exocyst complex. Finally, the tagged cell lines showed very similar proliferation rates to one another (Figure S3A). We conclude that addition of C-terminal tags to these subunits does not interfere with normal protein-protein interactions, nor – since the cells are viable and proliferate – with the biological function of the exocyst.

We took advantage of the sfGFP tag to compare relative expression levels of individual exocyst subunits in NMuMG cells. Surprisingly, as shown in Figure 1F, these levels are not equimolar. In particular, Sec5 and Sec8 are expressed at super-stoichiometric levels compared to the other 3 subunits (corrected where appropriate for heterozygosity). Sec8-GFP in particular was ~3-fold higher than expected. One potential explanation is that addition of the sfGFP tag stabilizes these proteins. However, blotting of cell lysates for Sec8 from 2 heterozygous Sec8-GFP clones showed that untagged and tagged alleles are expressed at the same levels (Figure S1G). These data suggest that in addition to forming exocyst complexes a surplus of free Sec8 and Sec5 must be present in cells. Whether they participate in other protein-protein interactions or have independent functions remains to be investigated.

Connectivity of the mammalian exocyst

It has been proposed that exocyst in budding yeast is a stable octamer comprised of two subcomplexes (SC1: Sec3, Sec5, Sec6, Sec8 and SC2: Exo70, Exo84, Sec10, Sec15) (Heider et al., 2016; Mei et al., 2018). To investigate the subunit connectivity in mammalian exocyst we silenced Sec8 in Exo70-GFP cells using a previously characterized hairpin RNA (Ahmed and Macara, 2017), then captured the complex on GFP-trap beads and performed quantitative full scan LC-MS/MS. Experiments were performed 3 d post-transduction of shRNAs, before apoptosis occurs, and loss of Sec8 was confirmed by western blot analysis. Interestingly, only proteins corresponding to SC2 were recovered; those from SC1 were absent (Figure 2A and S2B). Loss of Sec8 also strongly reduced detection of RalA and RalB, which bind not only to Sec5 in SC1 but also to Exo84 in SC2 (Figure S2B).

Conversely, we silenced Sec10 expression (Ahmed and Macara, 2017) by RNAi and captured Sec3GFP then subjected the precipitate to immunoblotting for Sec6, Sec8, Exo70 and Exo84 (Figure 2B and S2H, I). In this experiment components of SC1 (Sec6, Sec8) co-precipitated with Sec3, but not those of SC2 (Exo70, Exo84). Together, these data argue that the mammalian exocyst connectivity is very similar to that in yeast, with 2 subcomplexes, each of which needs to be intact for interaction with the other, and that loss of one subunit disrupts the stability only of its cognate subcomplex.

To test the functionality of the subcomplexes we asked if they can associate with the plasma membrane independently or only as an octameric complex. Association with basal membrane was assessed by TIRF microscopy. Subconfluent cells were used because vesicle fusion frequency at the basal membrane decreased substantially with confluency, when vesicles are redirected to apical junctions (Kreitzer et al., 2003). Both Sec3-GFP (SC1) and Exo70-GFP (SC2) were detected as fluorescent puncta in the unperturbed cell lines. Unexpectedly, however, when Sec10 (in SC2) was silenced Sec3-GFP remained detectable on the basal membrane, although Exo70-GFP was lost (Figure 2C,D). A similar experiment using the Sec5-GFP cell line showed no impact of silencing Sec10 on the association of Sec5 with the membrane (Figure 2E). Conversely, in a double knock-in cell line, silencing of either Sec8 or Sec3 (both in SC1; Figure S2C) caused the loss of Sec5-Sc or Sec5-Halo (SC1) but not Exo70-GFP (SC2) from the membrane (Figure 2F, G, S2J). Consistent results were also

obtained when Exo70 was deleted by Cas9-mediated gene editing: Sec8 (in SC1) was retained at the membrane (Figure S2F, G, K). From these data we conclude that each subcomplex remains intact and can associate normally with the plasma membrane in the absence of the other subcomplex.

Exocyst dynamics during vesicle delivery and fusion

Do all exocyst subunits arrive at the plasma membrane together with an exocytic vesicle, or do the subcomplexes or individual subunits arrive separately? To address this question we first transfected NMuMG cells with vectors to express mApple-Rab11 as a vesicle marker plus VAMP2-pHluorin, a vesicle-targeted pH-sensitive GFP that becomes highly fluorescent at the moment of vesicle fusion with the plasma membrane. Arrival of Rab11+ vesicles at the membrane can then be correlated with the fusion event by 2-channel time-lapse TIRF microscopy (Figure 3A). A typical kymograph is shown in Figure 3B, and analysis of multiple events provided a median value of -14.5 sec for arrival (Figure 3C). We next asked if vesicle fusions require exocyst, from measurements of events/min/field in cells separately depleted of each of 5 subunits (Figure S2C-G). Because silencing of Exo70 by shRNA was not efficient we used gRNA targeted gene disruption for this subunit (Figure S2J). In each case, loss of expression caused a significant reduction in fusion events (Figure 3D), confirming the importance of exocyst for vesicle delivery and fusion at the plasma membrane.

Based on this foundation, we simultaneously tracked exocyst subunit arrival and vesicle fusion using our GFP knock-in cell lines transfected with transferrin receptor fused to pHuji, a pH-sensitive RFP (TfR-pHuji). Representative kymographs are shown in Figure 3E, and data are quantified in Figure 3F. Interestingly, the 4 tested subunits (Sec3, Sec5, Sec6, Exo70) all arrive on average with median times of 10 - 14 sec prior to fusion (means = 14–17 sec; s.e.m. ~1 sec), which is close to the arrival time of the Rab11+ vesicles. This concordance is similar to that observed in budding yeast (Donovan and Bretscher, 2015), and suggests that exocyst arrives at the plasma membrane with the vesicles, rather than being preassembled on the membrane.

We next asked when exocyst subunits disappear from the fusion site. Sec5, Sec6 and Exo70 each depart with a median time of about 1.3 sec post-fusion (means 1.4 – 3sec,

s.e.m., 0.2 – 0.4 sec). Unexpectedly, however, (Figure 3G) Sec3 showed anomalous behavior with a median departure time of 0.4 sec prior to fusion (mean -1.5 sec, s.e.m., 0.38 sec), significantly different from the other subunits. This result is consistent with the reduced enrichment of Sec3-GFP detected at intercellular junctions (Figure 1D), and implicates Sec3 in a unique function associated with vesicle fusion. An alternative interpretation is that Sec3-GFP fusion might be only partially functional, with defective binding to the exocyst complex. We do not believe this to be the case, however, because the Sec3-GFP cell line proliferates normally, as compared to Sec8-GFP cells (Figure S3A), and the abundance of Sec5-Halo at the plasma membrane is identical in lines that express Sec3-GFP versus Sec8-GFP, which does not exhibit anomalous behavior (Figure S3B). Furthermore, we did not observe any differences in exocyst subunit interactions whether we used heterozygous Sec3-GFP or homozygous Sec3-Sc (Figure S3C, D). However, we were limited in our ability to employ Sec3-Sc for imaging experiments due to rapid photobleaching of the mScarlet fluorophore.

Coincidence measurements between exocyst subunits by TIRF

We next tested the arrival of different subunits with respect to each other. Using our double knock-in cell lines Sec8-sfGFP+Sec5-Halo or Exo70-sfGFP+Sec5-Halo we assessed the normalized fluorescence intensity trajectories with high time resolution to determine if the two fluorophores arrive at the plasma membrane simultaneously. Sec8-sfGFP and Sec5-Halo almost always arrived in the TIRF field together; however, Exo70-sfGFP and Sec5-Halo show a median delay of 77ms (95% CI: 0-300 ms) (Figure 4A-B). Importantly, this small but significant delay between SC1 and SC2 subunits could not have been detected by comparing single subunit versus vesicle fusion arrival times, as described in Figure 3 and in other studies (Donovan and Bretscher, 2015).

We also measured residency times for exocyst subunits on the plasma membrane. Both Exo70-sfGFP + Sec5-Halo and Sec8-sfGFP + Sec5-Halo pairs could be traced together for ~12-14s (Figure 4C), and these durations were similar to that of vesicle residency at the plasma membrane as assessed using Rab11-mApple (Figure 3C, 4D). These observations indicate that while association between SC1 subunits Sec5 and Sec8 is stable and they arrive together at the membrane, association between SC1 and SC2 is dynamic and

they can arrive independently at (or near) the plasma membrane. Nevertheless, once at the plasma membrane SC1 and 2 remain associated, with a similar residency time to that of the vesicles.

Single molecule approach to quantifying exocyst subunit interactions

Whether vesicles destined for the plasma membrane are associated with intact exocyst complexes or with only a subset of exocyst subunits remains controversial. To measure protein-protein interactions between Sec5-Sec3, Sec5-Sec8, and Sec5-Exo70 pairs throughout the cells rather than just at the plasma membrane we used single molecule counting.

First, we needed to determine the stoichiometry of fluorescent dye binding to Halo, as this parameter has not been previously reported. To address this issue, we created a YFP-Halo fusion protein, expressed it in NMuMG cells (Figure S4H) and added Halo dye (J585-HTL) at different concentrations for various periods of time. Flow cytometry showed a strong linear correlation between YFP and dye fluorescence (Figure S4I). Next, cells were ruptured in a small volume, then cleared by centrifugation, and lysates were spread onto coverglasses for single particle counting by two-color TIRFM (Figure 5A). Maximum fractional labeling efficiency was 0.40 +/- 0.014 after 1.5 hrs, and increasing this time to 18 hrs did not increase fractional labeling beyond 0.4 (Figure S4 J, K). A value of 0.34 was used to correct all subsequent data for Halo-tagged subunit interactions, as we used a ligand concentration of 150nM.

Next, lysates from double knock-in cells expressing Sec5-Halo plus Sec3-GFP, Sec8-GFP, or Exo70-GFP were rapidly spread on coverslips and co-localization in single particles was quantified as described above (Figure 5B). The majority of spots detected on the glass contained only single molecules of each species, as assessed by photobleaching, thus enabling a reliable assessment of fractional inter-subunit binding (Figure 5C, Figure S4D-E). Sec3 counts were corrected for heterozygosity. An AKT-Halo fusion, expressed in cells at a similar concentration to the endogenous Exo70-GFP fusion (Figure S4A-B), was used as a negative control to correct for chance colocalization. At the low fluorophore concentrations present, overlap was only 5 – 8% (Figure 5D).

Coincidence within the diffraction limit between Sec8-GFP and Sec5-Halo was much higher, at ~70% (Figure 5D, Figure S4C). Surprisingly, however, only ~40% of Sec3- and Exo70-GFP molecules colocalized with Sec5-Halo (Figure 5D). Conversely, colocalization of Sec5-Halo to Sec3-GFP or Exo70-GFP was even lower, at ~30%, most likely because Sec5 is expressed at a significantly higher level than Sec3 or Exo70 (Figure 1F). These results were corroborated by co-immunoprecipitation of Sec8GFP with ~80% of total Sec6 (in SC1) but only ~30% of total Exo70 (in SC2) (Figure S4F, G). Together, these data suggest that some subunits within a subcomplex (Sec5, Sec6 and Sec8 in SC1) interact stably, but that Sec3 binding is substoichiometric, and similar to the weak interaction between subcomplex-es.

Because Sec3 binds to other SC1 subunits so weakly, we asked if it is required for subcomplex stability. Sec3 or Sec6 (as a positive control) were efficiently silenced and Sec5/Sec8 interactions were measured by single molecule counting, corrected for sub-stoichiometric Halo labeling. Surprisingly, both perturbations strongly reduced Sec5/Sec8 binding (Figure 5E-F). These data suggest that Sec3 is essential for the assembly of SC1 (and perhaps interaction with SC2), but not for maintenance of the Sec5/6/8 heterotrimer once it has formed. This idea is consistent with the early departure of Sec3 from the exocyst complex prior to vesicle fusion (Figure 3E, G)

Fluorescence cross-correlation spectroscopy of exocyst subunits suggests that a fraction of the complex is pre-assembled

As an independent approach to determine the fraction of SC1 and SC2 subunits associated with each other we performed in-cell dual-color FCCS. We assessed co-diffusing fractions for Exo70-GFP, Sec8-GFP or Sec3-GFP with Sec5-Halo labeled with JF-646-haloligand in the cytosol or at the basal plasma membrane (Eq 3). About 70% ± 2.9% (*s.e.m)* of Sec8GFP was coupled to Sec5Halo in the cytosol and 64% ± 2.2% in the plasma membrane (Figure 6A-E), an abundance similar to that assessed by single molecule counting (Figure 5D). Sec3-GFP/Sec5-Halo coupling was 51% ± 2.9% in the cytoplasm and 44% ± 2.6% in the plasma membrane (numbers corrected for heterozygosity and a Halo labeling efficiency of 34% at 150nM ligand concentration) (Figure 6C-E, S4H-K). We also assessed the associa-

tion between SC1 and SC2 from the Exo70-GFP Sec5-Halo pair, with 48% ± 5.8% of the cytosolic fractions and 39% ± 7.0% of the membrane fractions co-diffusing (Figure 6A).

Data fitting (Eqs 1 and 2), revealed two diffusion components, with the slower diffusing (49% ± 10%) GFP-tagged population (D = 0.54μm^2/s ± 0.26; cyto and 0.50μm^2/s ± 0.31; PM) being common among all the subunits and cross-correlating. The faster component, which does not cross-correlate has a median diffusion rate of 14.5μm^2/s both in the cytosol and plasma membrane, reminiscent of freely diffusing molecules in cells (Gura Sadovsky et al., 2017). Importantly, Exo70-GFP, Sec8-GFP and Sec3-GFP did not show any cross-correlation with the negative control, Akt-Halo (Figure 6A-C). From these experiments we conclude that at least half of the exocyst subunits in the cells are pre-assembled in the cytosol and likely arrive at the plasma membrane with the vesicle, while the remaining subunits are not in a stable complex.

Diffusivity of exocyst subunits at the plasma membrane

The weak association of Sec3-GFP with intercellular junctions (Figure 1D) suggests that this subunit has unique properties. Consistently, we also found that localization of Sec3-GFP at the plasma membrane is significantly lower than that of its subcomplex partners (Figure 1D, 7A-B). These results, together with the observation that Sec3-GFP leaves the docked complex prior to vesicle fusion and before the other subunits (Figure 3G), suggests that Sec3 interacts unusually weakly with the complex. To further test this possibility, we measured diffusivity of the subunits at the plasma membrane by tracking individual particle trajectories, and calculated their mean squared displacements (Figure 7C). Sec3-GFP diffusion was anomalous with a median 0.12 $\mu m^2 s^{-1}$ (95% CI: 0.07-0.25) MSD compared to other subunits, which ranged from medians of 0.02 $\mu m^2 s^{-1}$ (95% CI: 0.02-0.03) to 0.08 $\mu m^2 s^{-1}$ (95% CI: 0.06-0.11) (Figure 7D-E). Total displacement measurements showed that Sec3-GFP motion was higher than that of other subunits, with a median of 0.21μm (95% CI: 0.21-0.22) as compared to Sec8-GFP or Exo70-GFP (median 0.10μm; 95% CI: 0.09-0.1), and Sec5-Halo (median 0.07μm; 95% CI: 0.075-0.078) (Figure S5A). We conclude that Sec3 interacts with the complex with unusually low affinity, suggesting that it might be the limiting factor in the formation of the octamer.

Quantification of the of exocyst molecules present during vesicle tethering

To better understand how exocyst tethers vesicles to the membrane, we quantified the number of complexes at tethered vesicles before fusion. Stepwise bleaching was not detected, suggesting there were large number of molecules present. Instead, we measured by ratio comparison to fluorescent standards (Wu et al., 2008). We fused different numbers (1, 2 or 3) of sfGFP in tandem to the c-terminus of CD86, a monomeric, plasma membrane-localized protein (Latty et al., 2015) and determined their photobleaching steps and initial intensities (I_o). These values were then used to generate a standard curve with coefficient of determination >0.99 (Figure 7F-G). To further ensure that we were measuring monomeric CD86, we immunostained fixed cells with anti-GFP antibodies conjugated to biotin and probed for photobleaching steps using streptavidin-ATTO488 (Figure S5B-D). These experiments confirmed that our constructs were behaving as expected. We also empirically determined the PFS of our objective and limited our analysis to objects that were at least resolved by a distance of 5 pixels on the camera to measure peak intensities (Figure S5B-I).

To calculate the numbers of exocyst subunits at sites of vesicle fusion, we expressed the TfR-pHuji construct in the exocyst-GFP knock-in cell lines and measured the peak intensities of well resolved particles of exocyst subunits at fusion sites (Figure 7H-I). We estimate approximately 9 molecules of each exocyst subunits are present with each vesicle during tethering (Figure 7I), slightly less than that predicted for budding yeast (Picco et al., 2017). The coefficient of variation (CV) in our calculations between each subunit was 7.88%. The CV for each subunit ranged between 30-48%, which is reasonable given ~27% of the variation can come from GFP measurements alone (Taniguchi et al., 2010).

DISCUSSION

A major goal of cell biology is to quantitatively assess the dynamics of molecular processes in living cells. This goal has often been confounded by perturbations introduced through over-expression of gene products, and by imaging limitations. In this study, we report the first quantitative analysis of endogenous exocyst dynamics in mammalian cells. We used CRISPR/Cas9 mediated gene editing to incorporate fluorescent tags at the C-termini of 5

exocyst subunits in NMuMG cells and assessed their connectivity and abundance. We employed fast TIRF imaging of these endogenous molecules to unravel arrival and departure times at vesicle fusion sites, and used single-molecule approaches to estimate the fractional binding and diffusivity of exocyst subunits, and the number of subunit molecules per tethered vesicle. Together, these complementary approaches enable a single cell biochemistry that is broadly applicable, and in this study has provided new and comprehensive insights into mammalian exocyst function.

Previously, we reported that Par3 interacts with exocyst in NMuMG cells and is required for membrane protein recruitment to lateral membranes and tight junctions (Ahmed and Macara, 2017). However, Par3 is absent from the basal membrane, and is unlikely to be involved in recruitment to this region of the cell cortex. Indeed, when we expressed mApple-Par3 in the knock-in cell lines, no signal was detectable at the basal surface by TIRFM; and silencing of Par3 expression did not reduce vesicle fusion frequency there (unpublished observations). Therefore, Par3 is not necessary for basal vesicle tethering and fusion, and whether there are different exocyst receptors for different regions of the cell remains to be investigated.

The assembly of exocyst remains controversial. In yeast, several lines of evidence suggest that the exocyst is a stable octameric complex, comprised of 2 subcomplexes, that is bound to vesicles prior to their arrival at the plasma membrane (Donovan and Bretscher, 2015; Heider et al., 2016). Others have proposed that Sec3 or Exo70 functions exclusively at the plasma membrane, and that the remaining exocyst subunits arrive on secretory vesicles (Boyd et al., 2004; Liu et al., 2018). In mammalian cells it has been proposed that 5 subunits on the plasma membrane interact with 3 subunits on incoming vesicles (Moskalenko et al., 2003). We found that subunit connectivity is conserved between yeast and mammals, but unexpectedly the two subcomplexes SC1 and SC2 can assemble and localize to the plasma membrane independently of each other. Moreover, FCCS showed that only about 50% of the SC1 and SC2 are associated with each other in the cytoplasm suggesting that the mammalian exocyst is not a stable octamer. Consistently, although arrival times at the plasma membrane are similar for all exocyst subunits and vesicles, there is a small (~80msec) delay between Sec5 (on SC1) and Exo70 (on SC2) suggesting that some of the

full exocyst complex assembles on the vesicle at or very near the plasma membrane. An alternative possibility is that the complex is pre-assembled but the tags do not enter the TIRF field simultaneously because of their distance from one another. We feel this explanation is unlikely, however, because – based on the yeast exocyst cryo-EM structure (Mei et al., 2018) – the C-terminal tags on Exo70 and Sec5 subunits are predicted to be closer together than those on Sec5 and Sec8.

After vesicle tethering, SNARE proteins assemble to form a *trans*-SNARE complex that mediates vesicle fusion (Hong and Lev, 2014). In yeast, Sec6 interacts with SNARES Sec9, Sso1, and Snc2 (orthologs of mammalian SNAP23/25, Syntaxins and Vamps respectively) (Dubuke et al., 2015; Morgera et al., 2012; Sivaram et al., 2005). Interestingly, in NMuMG cells we found that SNAP23 interacts with Exo70, but not with Sec6 or other subunits. No binding of Syntaxins to any of the exocyst subunits was detectable. One interpretation is that mammalian Exo70 facilitates SNARE complex formation by bringing SNAP23 to the vesicle tethering site, and the dissociation of Sec3 from the complex just prior to fusion then enables the SNARE complex to trigger membrane fusion (Figure 7J). Further studies using endogenously tagged SNARE proteins and high speed TIRFM will be required to further test this model. It will also be of great interest to determine the dynamics and function of exocyst regulators such as the Ral, Rab, and Rho family GTPases, and to investigate vesicle tethering at other domains such as the apical surface and intercellular junctions, using similar approaches.

Supplemental Information

Supplemental information includes 5 figures and 1 table.

Acknowledgements

This work was supported by NIH/NIGMS grant (GM070902) to I.G.M., NSERC Discovery Grant (RGPIN 2017 – 06030) to C.C.G., postdoctoral fellowships from the CIHR to S.M.A. and Grant-in-Aid for JSPS Research Fellow (17J40028) to H.N.F. Experiments and data analysis were performed in part through the use of the Vanderbilt Cell Imaging Shared Resources. Mass spectrometry experiments were performed using Vanderbilt MSRC Prote-

omics Lab. We acknowledge Jorge Rua Fernandez, Rabindra Shivnaraine, Goker Arpag, Marija Zanic, Tomas Kirchhausen and members of the Macara lab for helpful insights. We also thank Yasutsugu Takada, Shigeki Higashiyama and Shinji Fukuda (Ehime University, Japan) for their valuable support.

Author Contributions

S.M.A., H.N.F., Y.L, and W.H.M. conducted and analyzed the experiments. S.M.A., H.N.F., and I.G.M. designed the experiments. Y.L and C.G performed FCCS data analysis. S.M.A and I.G.M. wrote the paper.

Declaration of Interests

The authors declare no competing financial interests.

References

Adamo, J.E., Rossi, G., and Brennwald, P. (1999). The Rho GTPase Rho3 has a direct role in exocytosis that is distinct from its role in actin polarity. Molecular biology of the cell *10*, 4121-4133.

Ahmed, S.M., and Macara, I.G. (2017). The Par3 polarity protein is an exocyst receptor essential for mammary cell survival. Nature communications *8*, 14867.

Bacia, K., Petrasek, Z., and Schwille, P. (2012). Correcting for spectral cross-talk in dual-color fluorescence cross-correlation spectroscopy. Chemphyschem *13*, 1221-1231.

Bacia, K., and Schwille, P. (2007). Practical guidelines for dual-color fluorescence cross-correlation spectroscopy. Nat Protoc *2*, 2842-2856.

Baek, K., Knodler, A., Lee, S.H., Zhang, X., Orlando, K., Zhang, J., Foskett, T.J., Guo, W., and Dominguez, R. (2010). Structure-function study of the N-terminal domain of exocyst subunit Sec3. The Journal of biological chemistry *285*, 10424-10433.

Balakireva, M., Rosse, C., Langevin, J., Chien, Y.C., Gho, M., Gonzy-Treboul, G., Voegeling-Lemaire, S., Aresta, S., Lepesant, J.A., Bellaiche, Y.*, et al.* (2006). The Ral/exocyst effector complex counters c-Jun N-terminal kinase-dependent apoptosis in Drosophila melanogaster. Mol Cell Biol *26*, 8953-8963.

Boyd, C., Hughes, T., Pypaert, M., and Novick, P. (2004). Vesicles carry most exocyst subunits to exocytic sites marked by the remaining two subunits, Sec3p and Exo70p. The Journal of cell biology *167*, 889-901.

Brunet, S., and Sacher, M. (2014). Are all multisubunit tethering complexes bona fide tethers? Traffic *15*, 1282-1287.

Chen, X.W., Leto, D., Xiao, J., Goss, J., Wang, Q., Shavit, J.A., Xiong, T., Yu, G., Ginsburg, D., Toomre, D.*, et al.* (2011). Exocyst function is regulated by effector phosphorylation. Nature cell biology *13*, 580-588.

Chou, H.T., Dukovski, D., Chambers, M.G., Reinisch, K.M., and Walz, T. (2016). CATCHR, HOPS and CORVET tethering complexes share a similar architecture. Nat Struct Mol Biol *23*, 761-763.

Das, A., and Guo, W. (2011). Rabs and the exocyst in ciliogenesis, tubulogenesis and beyond. Trends in cell biology *21*, 383-386.
Donovan, K.W., and Bretscher, A. (2012). Myosin-V is activated by binding secretory cargo and released in coordination with Rab/exocyst function. Developmental cell *23*, 769-781.
Donovan, K.W., and Bretscher, A. (2015). Tracking individual secretory vesicles during exocytosis reveals an ordered and regulated process. The Journal of cell biology *210*, 181-189.
Dubuke, M.L., Maniatis, S., Shaffer, S.A., and Munson, M. (2015). The Exocyst Subunit Sec6 Interacts with Assembled Exocytic SNARE Complexes. The Journal of biological chemistry *290*, 28245-28256.
Dubuke, M.L., and Munson, M. (2016). The Secret Life of Tethers: The Role of Tethering Factors in SNARE Complex Regulation. Front Cell Dev Biol *4*, 42.
Fotso, P., Koryakina, Y., Pavliv, O., Tsiomenko, A.B., and Lupashin, V.V. (2005). Cog1p plays a central role in the organization of the yeast conserved oligomeric Golgi complex. The Journal of biological chemistry *280*, 27613-27623.
Friedrich, G.A., Hildebrand, J.D., and Soriano, P. (1997). The secretory protein Sec8 is required for paraxial mesoderm formation in the mouse. Dev Biol *192*, 364-374.
Grimm, J.B., Muthusamy, A.K., Liang, Y., Brown, T.A., Lemon, W.C., Patel, R., Lu, R., Macklin, J.J., Keller, P.J., Ji, N*., et al.* (2017). A general method to fine-tune fluorophores for live-cell and in vivo imaging. Nat Methods *14*, 987-994.
Guo, W., Grant, A., and Novick, P. (1999). Exo84p is an exocyst protein essential for secretion. The Journal of biological chemistry *274*, 23558-23564.
Guo, W., Tamanoi, F., and Novick, P. (2001). Spatial regulation of the exocyst complex by Rho1 GTPase. Nature cell biology *3*, 353-360.
Gura Sadovsky, R., Brielle, S., Kaganovich, D., and England, J.L. (2017). Measurement of Rapid Protein Diffusion in the Cytoplasm by Photo-Converted Intensity Profile Expansion. Cell Rep *18*, 2795-2806.
He, B., Xi, F., Zhang, X., Zhang, J., and Guo, W. (2007). Exo70 interacts with phospholipids and mediates the targeting of the exocyst to the plasma membrane. The EMBO journal *26*, 4053-4065.
Heider, M.R., Gu, M., Duffy, C.M., Mirza, A.M., Marcotte, L.L., Walls, A.C., Farrall, N., Hakhverdyan, Z., Field, M.C., Rout, M.P*., et al.* (2016). Subunit connectivity, assembly determinants and architecture of the yeast exocyst complex. Nat Struct Mol Biol *23*, 59-66.
Heider, M.R., and Munson, M. (2012). Exorcising the exocyst complex. Traffic (Copenhagen, Denmark) *13*, 898-907.
Hong, W., and Lev, S. (2014). Tethering the assembly of SNARE complexes. Trends in cell biology *24*, 35-43.
Hutagalung, A.H., Coleman, J., Pypaert, M., and Novick, P.J. (2009). An internal domain of Exo70p is required for actin-independent localization and mediates assembly of specific exocyst components. Molecular biology of the cell *20*, 153-163.
James, J.R., Oliveira, M.I., Carmo, A.M., Iaboni, A., and Davis, S.J. (2006). A rigorous experimental framework for detecting protein oligomerization using bioluminescence resonance energy transfer. Nat Methods *3*, 1001-1006.
Kreitzer, G., Schmoranzer, J., Low, S.H., Li, X., Gan, Y., Weimbs, T., Simon, S.M., and Rodriguez-Boulan, E. (2003). Three-dimensional analysis of post-Golgi carrier exocytosis in epithelial cells. Nature cell biology *5*, 126-136.
Latty, S.L., Felce, J.H., Weimann, L., Lee, S.F., Davis, S.J., and Klenerman, D. (2015). Referenced Single-Molecule Measurements Differentiate between GPCR Oligomerization States. Biophys J *109*, 1798-1806.
Liu, D., Li, X., Shen, D., and Novick, P. (2018). Two subunits of the exocyst, Sec3p and Exo70p, can function exclusively on the plasma membrane. Molecular biology of the cell *29*, 736-750.
Liu, D., and Novick, P. (2014). Bem1p contributes to secretory pathway polarization through a direct interaction with Exo70p. The Journal of cell biology *207*, 59-72.

Luo, G., Zhang, J., and Guo, W. (2014). The role of Sec3p in secretory vesicle targeting and exocyst complex assembly. Molecular biology of the cell *25*, 3813-3822.
Mei, K., Li, Y., Wang, S., Shao, G., Wang, J., Ding, Y., Luo, G., Yue, P., Liu, J.J., Wang, X.*, et al.* (2018). Cryo-EM structure of the exocyst complex. Nat Struct Mol Biol *25*, 139-146.
Morgera, F., Sallah, M.R., Dubuke, M.L., Gandhi, P., Brewer, D.N., Carr, C.M., and Munson, M. (2012). Regulation of exocytosis by the exocyst subunit Sec6 and the SM protein Sec1. Molecular biology of the cell *23*, 337-346.
Moskalenko, S., Tong, C., Rosse, C., Mirey, G., Formstecher, E., Daviet, L., Camonis, J., and White, M.A. (2003). Ral GTPases regulate exocyst assembly through dual subunit interactions. The Journal of biological chemistry *278*, 51743-51748.
Murthy, M., Ranjan, R., Denef, N., Higashi, M.E., Schupbach, T., and Schwarz, T.L. (2005). Sec6 mutations and the Drosophila exocyst complex. J Cell Sci *118*, 1139-1150.
Pathak, R., Delorme-Walker, V.D., Howell, M.C., Anselmo, A.N., White, M.A., Bokoch, G.M., and Dermardirossian, C. (2012). The microtubule-associated Rho activating factor GEF-H1 interacts with exocyst complex to regulate vesicle traffic. Developmental cell *23*, 397-411.
Picco, A., Irastorza-Azcarate, I., Specht, T., Boke, D., Pazos, I., Rivier-Cordey, A.S., Devos, D.P., Kaksonen, M., and Gallego, O. (2017). The In Vivo Architecture of the Exocyst Provides Structural Basis for Exocytosis. Cell *168*, 400-412 e418.
Rivera-Molina, F., and Toomre, D. (2013). Live-cell imaging of exocyst links its spatiotemporal dynamics to various stages of vesicle fusion. The Journal of cell biology *201*, 673-680.
Roumanie, O., Wu, H., Molk, J.N., Rossi, G., Bloom, K., and Brennwald, P. (2005). Rho GTPase regulation of exocytosis in yeast is independent of GTP hydrolysis and polarization of the exocyst complex. The Journal of cell biology *170*, 583-594.
Shivnaraine, R.V., Fernandes, D.D., Ji, H., Li, Y., Kelly, B., Zhang, Z., Han, Y.R., Huang, F., Sankar, K.S., Dubins, D.N.*, et al.* (2016). Single-Molecule Analysis of the Supramolecular Organization of the M2 Muscarinic Receptor and the Galphai1 Protein. J Am Chem Soc *138*, 11583-11598.
Sivaram, M.V., Saporita, J.A., Furgason, M.L., Boettcher, A.J., and Munson, M. (2005). Dimerization of the exocyst protein Sec6p and its interaction with the t-SNARE Sec9p. Biochemistry *44*, 6302-6311.
Taniguchi, Y., Choi, P.J., Li, G.W., Chen, H., Babu, M., Hearn, J., Emili, A., and Xie, X.S. (2010). Quantifying E. coli proteome and transcriptome with single-molecule sensitivity in single cells. Science *329*, 533-538.
TerBush, D.R., Maurice, T., Roth, D., and Novick, P. (1996). The Exocyst is a multiprotein complex required for exocytosis in Saccharomyces cerevisiae. The EMBO journal *15*, 6483-6494.
Torres, M.J., Pandita, R.K., Kulak, O., Kumar, R., Formstecher, E., Horikoshi, N., Mujoo, K., Hunt, C.R., Zhao, Y., Lum, L.*, et al.* (2015). Role of the Exocyst Complex Component Sec6/8 in Genomic Stability. Mol Cell Biol *35*, 3633-3645.
Ungar, D., Oka, T., Vasile, E., Krieger, M., and Hughson, F.M. (2005). Subunit architecture of the conserved oligomeric Golgi complex. The Journal of biological chemistry *280*, 32729-32735.
Willett, R., Kudlyk, T., Pokrovskaya, I., Schonherr, R., Ungar, D., Duden, R., and Lupashin, V. (2013). COG complexes form spatial landmarks for distinct SNARE complexes. Nature communications *4*, 1553.
Wu, B., and Guo, W. (2015). The Exocyst at a Glance. J Cell Sci *128*, 2957-2964.
Wu, H., Turner, C., Gardner, J., Temple, B., and Brennwald, P. (2010). The Exo70 subunit of the exocyst is an effector for both Cdc42 and Rho3 function in polarized exocytosis. Molecular biology of the cell *21*, 430-442.
Wu, J.Q., McCormick, C.D., and Pollard, T.D. (2008). Chapter 9: Counting proteins in living cells by quantitative fluorescence microscopy with internal standards. Methods Cell Biol *89*, 253-273.
Yakir-Tamang, L., and Gerst, J.E. (2009). A phosphatidylinositol-transfer protein and phosphatidylinositol-4-phosphate 5-kinase control Cdc42 to regulate the actin cytoskeleton and secretory pathway in yeast. Molecular biology of the cell *20*, 3583-3597.

Yamashita, M., Kurokawa, K., Sato, Y., Yamagata, A., Mimura, H., Yoshikawa, A., Sato, K., Nakano, A., and Fukai, S. (2010). Structural basis for the Rho- and phosphoinositide-dependent localization of the exocyst subunit Sec3. Nat Struct Mol Biol *17*, 180-186.
Yeaman, C., Grindstaff, K.K., and Nelson, W.J. (2004). Mechanism of recruiting Sec6/8 (exocyst) complex to the apical junctional complex during polarization of epithelial cells. J Cell Sci *117*, 559-570.
Zhang, X., Bi, E., Novick, P., Du, L., Kozminski, K.G., Lipschutz, J.H., and Guo, W. (2001). Cdc42 interacts with the exocyst and regulates polarized secretion. The Journal of biological chemistry *276*, 46745-46750.
Zhang, X., Orlando, K., He, B., Xi, F., Zhang, J., Zajac, A., and Guo, W. (2008). Membrane association and functional regulation of Sec3 by phospholipids and Cdc42. The Journal of cell biology *180*, 145-158.
Zhang, Z., Yomo, D., and Gradinaru, C. (2017). Choosing the right fluorophore for single-molecule fluorescence studies in a lipid environment. Biochim Biophys Acta *1859*, 1242-1253.

FIGURE LEGENDS

Figure 1. Establishment and Validation of Tagged Exocyst Subunit Cell Lines.

(A) Schematic showing region of subunit gene targeted by sgRNA and tags to be inserted C-terminally, in-frame with the coding region.

(B) Strategy to isolate CRISPR/Cas9-mediated sfGFP-tagged clones of exocyst subunits in NMuMG cells.

(C) Western blots with subunit specific antibodies show successful incorporation of sfGFP in both alleles (Exo70, Sec5 and Sec8), or in one allele (Sec3 and Sec6). A shRNA specific to Sec3 was used to confirm the identity of multiple bands in the blot.

(D) Confocal images of live wild-type NMuMG cells and endogenously tagged Sec3-GFP, Sec5-GFP, Sec6-GFP, Sec8-GFP and Exo70-GFP cell lines. Scale bar = 10μm.

(E) Protein-protein interaction heat map for endogenous Sec3-GFP, Sec5-GFP and Exo70-GFP pull-down using GFP-Trap nanobodies. Yellow indicate baits, blue the protein identified with high confidence, and grey denotes preys that were not identified with all three baits.

(F) Western blot analysis to assess relative abundance of exocyst subunits fused to sfGFP, using anti-GFP antibodies. Gapdh used as loading control. Y-axis shows the ratio of GFP/Gapdh.

See also Figure S1 and Table S1.

Figure 2. Mammalian Exocyst Complex Comprises Two Subcomplexes that Can Localize to the PM Independently.

(A) Quantitative full scan LC-MS/MS analysis of endogenous Exo70-GFP pull-downs from intact or Sec8-depleted cells. Inputs for the samples were calibrated and normalized using MRM-MS anal-

ysis on the same samples. Schematic shows the experimental design in which Exo70-GFP was captured using GFP-Trap beads and Sec8 was depleted by shRNA.

(B) Heat map summarizing relative binding of Sec6, Sec8, Exo70, and Exo84 to Sec3-GFP in Sec10-depleted cells compared to control shRNA treated cells, as assessed by western blot. Also see Figure S2H-I.

(C) TIRFM images of Exo70-GFP and Sec3-GFP in Control or Sec10 shRNA treated cells. Scale bars 20μm.

(D) Quantification of relative fluorescence intensities in C.

(E) Quantification of fluorescence intensities from TIRFM images of Sec5sfGFP cells treated with Control or Sec10 shRNA.

(F) TIRFM images of double knock-in NMuMG cells, showing localizations of Exo70-GFP and Sec5-mScarleti at the PM in Control, Sec8 shRNA and Sec3 shRNA treated cells. Scale bars = 20μm.

(G) Quantification of relative fluorescence intensities in D.

Center lines show the median; box limits indicate 25th and 75th percentiles; whiskers extend 1.5X the IQR from the 25th and 75th percentiles.

Also see Figure S2.

Figure 3. Sec3 Departs from the Exocyst Complex Prior to Vesicle Fusion.

(A) Schematic representation of the data. Black arrowhead shows arrival of the target protein, gray arrowhead shows departure, red arrowhead shows vesicle fusion events as demarcated by pH sensitive fluorophores, pHluorin or pHuji, fused to Vamp2 or Transferrin receptor, respectively.

(B) NMuMG cells were transduced with mApple-Rab11 and Vamp2-pHluorin lentivirus and imaged by TIRFM. Kymographs show arrival and departure of mApple-Rab11 and vesicle fusion, highlighted by Vamp2-pHluorin flashes. Speed = 5Hz. Scale bar = 5s.

(C) Distribution of mApple-Rab11 arrival times prior to vesicle fusions. Inset shows box and whisker plot; center line = median. Error bars = Tukey's range.

(D) Effects of exocyst subunits depletion on vesicle fusion activities in NMuMG cells assessed using Vamp2-pHluorin. n = 32, 32, 18, 22, 21, 22. *P* values compared to control.

(E) Kymographs showing itinerary of Sec3-GFP, Sec5-GFP, Sec6-GFP and Exo70-GFP subunits with respect to the vesicle fusion marker TfR-pHuji. Square images show snapshots in the green and red channels at the time of vesicle fusions. Scale bar = 5s.

(F-G) Quantification of exocyst subunit arrival and departure times at and from the vesicle fusion site shown in E. Data points shown as dots.

Center lines = medians; hinges extend from 25th and 75th percentiles. Statistical significance measured by Kruskal-Wallis test followed by Dunn's *post hoc* analysis.
Also see Figure S3

Figure 4. Coincidence Measurements Between Exocyst Subunit Pairs in the Same Subcomplex or Different Subcomplexes by TIRF in Live Cells.

(A) Fluorescence intensity trajectories (intensity values were normalized to a common scale) for the Sec5-Halo+JF585/Sec8-GFP pair, and Sec5-Halo+JF585/Exo70-GFP pair over 20 sec. The fluorophores were excited simultaneously and images captured at 12.5Hz (left). On the right, graphs show the displacement of the normalized intensities of the two fluorophores at each time point.

(B) Quantification of the delay in coincidence between Exo70-GFP and Sec5-Halo+JF585 or Sec8-GFP and Sec5-Halo, measured by TIRFM. Outliers are represented by black circles; data points are plotted as magenta circles.

(C) Distributions of the duration of the indicated subunits were together in the TIRF field.

(D) Comparison on the distribution of residence times of Rab11 and the indicated pairs of exocyst subunits. White circles = medians; box limits indicate the 25th-75th percentiles; whiskers extend 1.5X the interquartile ranges from 25th-75th percentiles; polygons represent density estimates of data and extend to extreme values. Statistical significance measured by Kruskal-Wallis test followed by Dunn's *post hoc* analysis.

Figure 5. Assessment of Fractional Binding of Exocyst Subunits Using Single Molecule Approach.

(A) Diagram showing experimental workflow.

(B) Cleared cell lysates from the indicated double knock-in cells were spread between quartz slides and glass coverslips for TIRF imaging. The GFP and Halo+JF585 fluorophores were excited simultaneously with 488nm and 561nm lasers at 12.5Hz for 40s. Scale bars = 1μm.

(C) Number of photobleaching steps detected for Sec5-Halo and Sec8-GFP in experiments shown in panel B.

(D) Quantification of the fraction of subunit "A" bound to (->) subunit "B" from experiments shown in panel B. Numbers of particles analyzed for each pair are shown in Figure S4C.

(E) Fraction of Sec5-Halo and Sec8-GFP bound to each other in Sec3 or Sec6 shRNA treated cells compared to control. Center line denotes mean.

(F) Western blot analysis of Sec3 and Sec6 shRNA knockdown efficiencies in the experiment shown in E.

Error bars denote ± *s.d.* Statistical significance was computed by one-way (D) or two-way (E) ANOVA, followed by Tukey's multiple comparison tests.
Also see Figure S4.

Figure 6. Dual-color FCCS of Exocyst Subunits in Membrane and Cytosol.

(A) Sec5-Halo and Exo70-GFP FCS measurements in the cytosol and the PM. Exo70-GFP and AKT-Halo fluorescence cross-correlation was used as negative control. HaloTag was labeled using JF646 Halo ligand (200 nM for 1.5h).

(B) Sec5-Halo and Sec8-GFP, or Sec8-GFP and AKT-Halo FCS measurements in the cytosol or the PM.

(C) Sec5-Halo and Sec3-GFP, or Sec3-GFP and AKT-Halo FCS measurements in the cytosol or the PM.

(D) Statistics of fraction of GFP-tagged exocyst subunit bound in the cytosol.

(E) Statistics of fraction of GFP-tagged exocyst subunit bound in the PM.

FCS measurements (dots = data points) were fitted (lines) to the model described in Methods (Eqs 1 and 2). Curves shown are representative take from a single cell. *p values* were calculated by one-way ANOVA followed by Tukey's *Post hoc* test.

Figure 7. Measurements of Diffusivity of Exocyst Subunits.

(A) TIRFM images of untagged wild-type or indicated exocyst subunits fused to sfGFP (top). Heat map of above images (bottom). Scale bar = 20μm.

(B) Quantification of exocyst subunits localization at the TIRF field. Membrane localization Index = Density of spots * Intensity of cells. Whiskers extend from min to max. Values for Sec3 and Sec6 were corrected for heterozygosity. n= 31, 13, 13, 13, 32.

(C) Particle tracking over time for the subunits indicated. For two color tracking, each channel was tracked using Imaris software tracking algorithm and overlaid. Graphs show mean squared displacements over time. Scale bar = 0.5μm (Sec3GFP) and 0.8μm (rest).

(D) Representation of data in B as geometric means of MSDs.

(E) Diffusion coefficients of the indicated subunits as measured from MSD over time. White circles show the medians; box limits indicate the 25th and 75th percentiles; whiskers extend 1.5 times the interquartile range from the 25th and 75th percentiles; polygons represent density estimates of data and extend to extreme values.

(F) Stepwise photobleaching of CD86 fused to one or two GFP molecules used to determine intensities of known numbers of GFP molecules.

(G) Standard curve for counting protein molecules, from intensities measured on CD86 fused to 1, 2 or 3 GFP molecules. Error bars = ± *SD*; pink shaded region denote 95% confidence band.

(H) Fluorescence landscape of Sec8sfGFP shows a typical resolvable distribution of molecules within an ROI from which intensity measurements were taken.

(I) Exocyst molecule counting at vesicle fusion sites. Intensity (y) was measured from the peak and converted to the number of molecules using the regression equation determined in G. Numbers for Sec3 and Sec6 were corrected for heterozygosity. Centers indicate median, box limits indicate 25th and 75th percentiles and whiskers extend 1.5x IQR from 25th and 75th percentiles. n = 96, 50, 51, 50, 58. Coeffient of variation = 47.9%, 35.2%, 39.2%, 34.3, 30.7% in the order indicated in the graph.

(J) Model of exocyst subunits assembly and vesicle tethering prior to fusion in mammalian system.

P values were computed using Kruskal-Wallis test followed by Dunn's multiple comparison tests.

Also see Figure S5

SUPPLEMENTARY FIGURES

Figure S1. Design and Validation of Gene-Edited Exocyst Cell Lines. Related to Figure 1.

(A) Schematic of designs for targeting vectors to insert sfGFP at the C-terminus of exocyst subunits Sec3, Sec5, Sec6 and Exo70 genes.. Targeting vector deletes the STOP codon and PAM sequence.

(B) Genotypes of Sec3-GFP clones using primer sets listed in STAR methods. Bottom panel shows sequencing of PCR product of the C-terminal region of clone 10.

(B-E) Genotypes of Sec5-GFP, Sec6-GFP and Exo70-GFP clones as indicated.

(F) Genotype of Sec5-Halo/Exo70-GFP double knock-in clones as indicated.

(G) Western blot of Sec8-GFP clones using either anti-Sec8 or anti-GFP antibodies. Gapdh antibodies used to assess loading.

(H) Western blot analysis and PCR genotyping of Sec5-mScarlet/Exo70-GFP double knock-in clones. Sec5-mScarlet expression was assessed using anti-RFP antibodies.

(I) Confocal images of Sec10-GFP and Sec15-GFP after gene editing and FACS. White arrowheads indicated cells with successful incorporation of sfGFP.

(J) Western blot analysis of Sec3-GFP, Sec5-GFP, Sec60GFP, Sec10-GFP and Sec15-GFP cell lines using anti-GFP antibodies. WT = wild type parental cells.

(K) Sec5-GFP or Exo70-GFP pulldown using GFP-Trap beads followed by immunoblot analysis to determine binding of native Sec8 (anti-Sec8 antibody) and SNAP23 (anti-SNAP23 antibodies). Pulldowns of Sec5-GFP or Exo70-GFP were assessed using anti-GFP antibodies.

Figure S2. Mammalian Exocyst Subunit Connectivity. Related to Figure 2.

(A) Exo70-GFP capture using GFP-Trap nanobodies. Shown are representative MRM spectra of intensity peaks features of the indicated Exo70 and sfGFP peptides in the control or Sec8shRNA treated cells.

(B) Quantifications of the area under the curve (AUC) for the indicated peptides for each protein species shown. Control pull-downs are denoted in blue whereas Sec8 depleted conditions are designated in red.

(C) Knockdown efficiencies of two independent shRNAs targeting Sec3-GFP. α-Tubulin used as loading control.

(D) Knockdown efficiency of Sec6 shRNA.

(E) Knockdown efficiency of Exo70 shRNA.

(F) Knockout efficiency with three independent guide RNAs targeting Exo70 gene loci in Exon1.

(G) Quantification of panel F.

(H) GFP-Trap pull-down of endogenous Sec3-GFP from untreated or Sec10 shRNA treated NMuMG cells. Western blots were immunoblotted with anti-GFP to detect Sec3-GFP, or with anti-Sec6, anti-Sec8 and anti-Exo70 antibodies to assess co-precipitations of unlabeled exocyst subunits.

(I) GFP-Trap pull-down of endogenous Sec8-GFP from untreated or Sec10 shRNA treated NMuMG cells. Blots were probed with anti-GFP to detect Sec8-GFP, or with anti-Exo84 antibodies to assess amount of co-precipitation of endogenous unlabeled Exo84.

(J) Quantification of fluorescence intensities from TIRFM images of Sec5-Halo and Exo70-GFP double knock-in cells treated with Control or Sec8 shRNAs. Sec5-Halo was labeled with JF585 Halo ligand.

(K) Fluorescence intensity quantifications of Sec8-GFP from TIRFM images in untreated or Exo70 knockout cells.

Center lines show the medians; box limits indicate the 25th and 75th percentiles as determined by R software; whiskers extend 1.5 times the interquartile range from the 25th and 75th percentiles, data points are plotted as dots. Statistical significance was assessed using one-way ANOVA followed by Sheffe's multiple comparison tests.

Figure S3. Functionality of Exocyst Knock-in Cell-Lines. Related to Figure 3.

(A) Cell proliferation of Sec8-GFP, Sec3-GFP, Sec8-GFP + Sec5-Halo and Sec3-GFP + Sec5-Halo knock-in cells over three days. Error bars indicate ± *s.d.* Statistical analysis was using one-way ANOVA to compare groups for each day.

(B) Comparison of Sec5-Halo fluorescence intensity at the bottom PM (PM) in double knock-in cells. Intensities were measured using TIRFM. Halo tag was labeled with JF585-HTL.

(C) Western blot analysis of Sec3-Scarlet+ Sec6-GFP double knock-in cells. Clone A1 is homozygous for Sec3. WT = wild-type parental NMuMG cells.

(D) GFP-Trap pull-down and western blots analysis from double knock-in cell lines expressing Sec3-GFP, or Sec3-Scarlet + Sec6-GFP. WT = wildtype cells, Cln = clone.

Figure S4. Fractional Interactions of Cellular Pools of Exocyst subunits. Related to Figure 5.

(A) AKT-Halo was expressed in Exo70-GFP cells as a negative control for interactions. Halotag was labeled with JF-646 HTL and and imaged to look at the distribution of expression prior to cell sorting. Scale bar = 20μm.

(B) Sec3-GFP, Sec8-GFP and Exo70-GFP knock-in cells were transduced with lentivirus expressing AKT-Halo, and sorted for similar expressed levels than Sec5-Halo. Halo was labeled with JF-646 HTL.

(C) Graph shows number of molecules analyzed in the data shown in Figure 5D.

(D) Typical distribution of the duration of fluorescence intensity of Sec8-GFP or Sec5-Halo+JF585 over 50s with microscope parameters as for experiments in Figure 5.

(E) Representative images of 0, 1 or 2 photobleaching steps detected by the step detection algorithm.

(F) Representative experiment where Sec8-GFP was captured using GFP nanobodies and immunoblotted with anti-Sec8, anti-GFP, anti-Sec6 or anti-Exo70 antibodies. Blots on the left show 2.4% input of the total lysate and the blot of the right shows pulldown with nanobodies.

(G) Quantification of the percentage of Sec6 and Exo70 bound to Sec8 from 3 independent experiment experiments.

(H) Schematic showing experimental design to determine Halo labeling efficiency in NMuMG cells. Halo fused to the C-terminus of of YFP was expressed in NMuMG cells using lentiviral expression system, and subsequently sorted for positive cells.

(I) Correlation between fluorescence intensities of YFP and Halo labeled with JF-646-HTL.

(J) Halo labeling efficiency across different concentrations (6.25, 25, 100, 150, and 400 nM) of HaloTag ligand conjugated to JF585 dye in NMuMG cells for 1.5h.

(K) Halo labeling efficiency after NMuMG cells were labeled with 100nM of HaloTag ligand conjugated to JF585 for 1h or 18h.

Figure S5. Determination of Criteria Used to Count Exocyst Subunit Molecules from Fluorescence Intensities. Related to Figure 7.

(A) Distribution of vector displacements between the first and last frames of the particle trace. Data are shown from >20,000 object for each exocyst subunit as indicated. Statistical significance was measured by Kruskal-Wallis non-parametric test followed by Dunn's post-hoc test.

Photobleaching steps of (B) CD86-1xsfGFP (C) CD86-2xGFP and (D) CD86-3xsfGFP in cells fixed with 3.7% paraformaldehyde followed by methanol and immunolabeled with anti-GFP-biotin antibodies and Streptavidin-ATTO488 dye.

(E) Fluorescence landscape showing point-spread function of a single tetraspec bead spread on glass.

(F) Fluorescence landscape of multiple tetraspec beads close together. Arrows point to two close but resolvable peaks from which individual intensities could be measured.

(G) 2D intensity plots of the peaks described in F.

(H) Intensity trace shown in panel is shifted to show minimal separation in pixel distance (5 pixels) that was used to measure intensities of the objects in cells.

(I) Distributions of average intensity traces over a 20nm bead (n=3) or a Sec5-GFP particle at vesicle fusion sites (n=5).

STAR Methods

Key Resources table.

Cell lines

Cell lines	***Source***	***Catalog no.***
NMuMG	ATCC	ATCC CRL-1636
HEK293T	ATCC	ATCC CRL-3216

Peptides used in MRM-MS

Uniprot ID	**Protein Name**	**Peptide Sequences**
Q8R3S6	Sec3_MOUSE	DLAVVDAK
		LNHFFEGVEAR
Q9D4H1	Sec5_MOUSE	LVLSQLPNFWK
		LFENYIELK
Q6KAR6	Sec6_MOUSE	NIFSVPEIVR
		LTDPSLLYLEVSTLVSK
O35382	Sec8_MOUSE	TYQSITER
		FIQEIEHALGLGPAK
Q3TPX4	Sec10_MOUSE	YFNEFLDGELK
		LSDPSDLPR
Q8R313	Sec15_MOUSE	FPFQDPDLEK
		HAAEGEIYTK
O35250	Exo70_MOUSE	HDFSTVLTVFPILR
		VTDYIAEK
Q6PGF7	Exo84_MOUSE	DFEGAVDLLDK
		QLTEVLVFELSPDR

Primers for genotyping

Primer #	**Exocyst Subunit**	**Primer direction**	**Sequence (5' -> 3')**
M12	Sec6	Forward	CTGAACGTGGCAAAGCTCCTTA
M13	Sec6	Reverse	GCAGACACAATCCACTCACTGG
M14	Sec6	Forward	GCCTCTGGACATGGCTGTAT
M15	Sec6	Reverse	GTTCATGCTGCCTTCTCTCC
M73	Sec5	Forward	AGCCCGTCACTGTCAGGATG
M74	Sec5	Reverse	ATGGGCATCTTTCTGCACCACC

M75	Sec5	Forward	AGAATTCCATAGGCACTGGCTT
M76	Sec5	Reverse	ACAGGGTACATATGCTGTGCTC
M81	Sec3	Forward	GGTGGTGTGGCACTCCATGC
M82	Sec3	Reverse	CAGCCGCTCGAAAACACAAG
M83	Sec3	Forward	CTGAGGGCCGAGACATGGAG
M84	Sec3	Reverse	CAATGAGCTAATGGGCAGCC
E21	Exo70	Forward	GGTATGGCAGCGTGCCCTTC
E22	Exo70	Reverse	GGGGCTCCTGGTTTGGGCAC

sgRNA sequences to generate knock-ins

Subunits	**sgRNA sequences (5' -> 3') PAM**
Sec3	ACTCTTTCCGTAGTGTTTGCTGG
Sec5	AAGAGCATCAGACATGGCGGTGG
Sec6	CCTATGTGTCTTTACTGTGTGG
Sec8	GAGTCTGTGGCCGTGCATACTGG
Sec10	TCTCAGAAGGCCTCGGTAATGGG
Sec15	TATTGTCTCACGACCAGTGCTGG
Exo70	GTGTTTCTGCCCAGTTCTGCCGG

Image analysis softwares

Software	**Version**	**Source**
Fiji	Ver 2.0.0-rc-64/1.51s	ImageJ
NIS Elements Ar	Ver 5.0.0 patch 2	Nikon Instruments
Imaris	Ver. 9.2 Full	Bitplane
Matlab	R2018a	MathWorks

Statistical softwares

Software	Version	Source
R-Studio Plugins: IPSUR and KMggPlot2	1.1.447	R-Studio, Inc
Prism 7	7.0d	Graphpad software, Inc
JASP	0.8.5.1	University of Amsterdam

Mass spectrometry analysis softwares

Software	Source
MaxQuant	Max Plank Institute of Biochemistry
Scaffold 4	Proteome Software, Inc
Skyline	MacCoss Lab, University of Washington

Plasmids constructs and other reagents

pIRESpuro2-CD86-mEos2 and pIRESpuro2-CTLA4-mEos2 were gifts from Mike Heilemann (Addgene plasmids # 98284 and 98285). mEos2 was replaced with superfolder GFP coding sequence (sfGFP), which was PCR amplified from sfGFP-N1, a gift from Micheal Davidson (Addgene plasmid # 54737), with flanking XmaI/NotI restriction enzyme sites and inserted at the AgeI/NotI site of the plasmid in frame with CD86. As such, the AgeI site at the beginning of sfGFP was destroyed and a new AgeI site created at the end of sfGFP before the stop codon, to enable insertion of subsequent tandem sfGFP coding sequences in frame. pEGFP-VAMP2 was a gift from Thierry Galli (Addgene plasmid # 42308). TfR-pHuji was a gift from David Perrais (Addgene plasmid # 61505). Superecliptic pHluorin (pHluorin2) was PCR amplified from VV063: 1xCox8-superecliptic pHluorin in fck, a gift from Adam Cohen (Addgene plasmid # 58500) to make VAMP2-pHluorin2. Halo-tag coding sequence was synthesized as a geneblock (IDT) to make VAMP2-Halo. AKT-Halo construct was generated by replacing mApple with HaloTag using the EcoRI/NdeI restriction sites at the C-terminal end of a pLVTHM-AKT-CA construct described previously (Ahmed and Macara, 2017). For CRISPR/Cas9-mediated gene editing, locus-specific 5’ and 3’ homology arms were synthesized as

gBlocks double-stranded gene fragments (IDT), or amplified by PCR. These gene fragments were designed to remove the stop codon from the gene ORF, delete the PAM sequence recognized by the cognate sgRNA, and to attach an in-frame tag (sfGFP, HaloTag or mScarleti). They were then cloned into LITMUS29 vector together with the appropriate tag either using Gibson assembly (NEB) or by conventional cloning using the following restriction sites: KpnI/PstI (Sec3), KpnI/EcoRI (Sec5), XbaI/BamHI (Sec6), KpnI/EcoRI (Sec8), BamHI/XhoI (Exo70).

The following hairpin RNA clones were purchased from the Sigma MISSION shRNA library: mouse Sec3 shRNA clones TRCN0000254147, TRCN0000254146 and TRCN0000254145, Sec6 shRNA clones TRCN0000111629, mouse Sec8 shRNA clones TRCN0000307390 and TRCN0000298307, mouse Sec10 shRNA clone TRCN0000093547, and Exo70 shRNA clone TRCN0000376796. Silencing effiiciencies of the shRNA were verified by immunoblotting analysis compared to a control shRNA targeting Luciferase. Exo70 sgRNA (5'-CACCGGTTGTCTGGCAGCTGGCTA-3') was cloned into lentiCRISPR-v2 at the BsmBI restriction site.

For immunoblotting, we used the following antibodies: mouse anti-Sec8 (Clone 14/Sec8, BD Biosciences), mouse anti-Sec6 (Clone 9H5, Novus Biologicals), Rabbit anti-Exo70 (Bethyl Laboratories), Rabbit anti-GFP (ThermoFisher Scientific), chicken anti-GFP (Abcam), goat anti-GFP-biotin (Abcam), rabbit anti-RFP (Rockland), mouse anti-α-tubulin (Clone DM1A, Sigma-Aldrich), rabbit anti-GAPDH (Clone 14C10, Cell Signaling Technology), mouse anti-RalA (Clone 8/Ral A, BD Transduction Laboratories). GFP-Trap®_MA beads were purchased from ChromoTek GmbH.

Other materials used in this paper were as follows. Q-VD-Oph (Sigma-Aldrich); ProLong® Live Antifade Reagent (Thermo Fisher Scientific). Trolox (Acros Organics) was used for live cell imaging. FluoroBright DMEM medium for live cell imaging was from Life Technologies. Fetal Bovine Serum (FBS) was from Atlantic Biologicals. JF585-Halo and JF646-Halo dyes were gifts from Luke Lavis, Janelia Farms HHMI Institute (Grimm et al., 2017).

Cell culture

NMuMG and HEK293T cells were obtained from ATCC. Cells were cultured in Dulbecco's Modified Eagle Medium (Life Technologies), supplemented with 10% FBS and 1X Penicillin/Streptomycin (Life Technologies) and maintained in culture as suggested by ATCC.

Lentiviral transductions and transient transfections

Lentivirus was produced by transfecting HEK293T cells with lentiviral packaging vectors pMD2.G and psPAX2 using calcium phosphate precipitation. Lentiviral transductions were with virus-conditioned medium collected from HEK293T cells 48h post-transfection. Xfect transfection reagent (Takara) was used to transiently transfect NMuMG cells, to create exocyst knock-in cell lines.

CRISPR/Cas9-mediated generation of knock-in cell lines

NMuMG cells were plated at 10^5 cells/well in 6 well plate 24 h before transfection. Cells were transfected with targeting vector (LITMUS29 backbone), sgRNA (Addgene plasmid #41824) and Cas9 expression vector (pCMVsp6-nls-hCas9-nls) a gift from Li-En Jao (UC – Davis), at an equimolar (550 fmol) ratio using Xfect transfection reagent according to the manufacture's protocol. The GFP positive cells were subsequently sorted on a FACSAriaIII (BD) 5 d post-transfection. After single cell cloning, insertions were confirmed by immunoblot analysis and PCR-based genotyping.

Stable cells

NMuMG cells transduced with shRNAs or sgRNA were selected using puromycin (2μg/ml). Cells infected with Vamp2-pHluorin, Vamp2-Halo or AKT-Halo were selected using Blasticidin (10μg/ml) or FACS.

Immunoprecipitation and quantitative western blot

NMuMG CRISPR cells lines expressing sfGFP-tagged exocyst subunits were grown to confluency in 100mm cell culture dishes. Cells were washed with PBS and lysed in 1ml lysis buffer containing 20mM HEPES; pH 7.4, 50mM NaCl, 2mM EDTA, 0.1% Triton X-100, supplemented with cOmplete™ mini EDTA-free protease inhibitor cocktails (Roche) and PhosStop (Roche). Cells were lysed in a rotator for 15 min at 4°C and debris removed by centrifugation at 16,000*xg*. For quantitative immunoprecipitation protein amounts were measured using a BCA assay (ThermoFisher Scientific) and small amount of lysates from each step (input, unbound, wash) were retained for analysis. Affinity purifications were performed with GFP-Trap_MA beads. Quantitative immunoblot analysis used secondary antibodies conjugated to IRDye® 680RD or 800CW (LI-COR), imaging blots with Odyssey CLx Infrared Scanner (LI-COR).

Affinity purification for mass spectrometry

Gene edited NMuMG cell lines were grown to confluency in 4 to 5 150mm cell culture dishes. Cells were washed 3x with 20ml PBS and lysed in 10ml lysis buffer described above, supplemented with cOmplete™ mini EDTA-free protease inhibitor cocktails (Roche), PhosStop (Roche) and NaF

(100mM; Sigma-Aldrich). Cells were harvested using a cell scraper followed by immediate freezing in liq N_2. Lysates were thawed and briefly sonicated on ice using a microtip sonicator (20s; Vibra-Cell), followed by centrifugation at 16,000*xg* for 10 min at 4°C to remove debris. Supernatants were transferred into 15ml conical tubes and baits captured on GFP-Trap®_MA beads by end over end mixing at 4°C for 30 min. Beads were separated using Magnetic Particle Concentrator (ThermoFisher Scientific), unbound supernatant aspirated followed by 3 x 1.5ml washes in the lysis buffer. Samples were eluted in 2x Laemmli sample buffer and heated to 95°C for 15 min and subsequently processed for mass spectrometry (MS) analysis).

Sample preparation for multiple reaction monitoring mass spectrometry

Affinity purification was performed as mentioned above and relative abundance of each exocyst subunits binding to the bait was compared across label free samples by multiple reaction monitoring mass spectrometry (MRM-MS). Quantified stable-isotope-peptides for quantitative MRM were obtained from JPT Peptide Technologies GmbH.

The quantified stable-isotope-labeled peptide standards were spiked into the sample of interest and peptides from the endogenous exocyst subunits quantified from the ratio of the labeled peak heights to the unlabeled.

Mass spectrometry

LC-MS/MS: Exocyst protein immunoprecipitations were run on a NuPAGE Bis-Tris gel, were stained with Novex colloidal Coomassie stain (Invitrogen), and destained in water. Coomassie stained gel regions were cut from the gel and diced into $1mm^3$ cubes. Proteins were treated for 30 minutes with 45 mM DTT, and available Cys residues were carbamidomethylated with 100mM iodoacetamide for 45 min. Gel pieces were further destained with 50% MeCN in 25mM ammonium bicarbonate, and proteins were digested with trypsin (10ng/uL) in 25mM ammonium bicarbonate overnight at 37°C. Peptides were extracted by gel dehydration with 60% MeCN, 0.1% TFA, the extracts were dried by speed vac centrifugation, and reconstituted in 0.1% formic acid.

Peptides were analyzed by LC-coupled tandem mass spectrometry (LC-MS/MS). An analytical column was packed with 20cm of C18 reverse phase material (Jupiter, 3 µm beads, 300Å, Phenomenox) directly into a laser-pulled emitter tip. Peptides were loaded on the capillary reverse phase analytical column (360 µm O.D. x 100 µm I.D.) using a Dionex Ultimate 3000 nanoLC and autosampler. The mobile phase solvents consisted of 0.1% formic acid, 99.9% water (solvent A) and 0.1% formic acid, 99.9% acetonitrile (solvent B). Peptides were gradient-eluted at a flow rate of 350

nL/min, using a 110-minute gradient. The gradient consisted of the following: 1-3min, 2% B (sample loading from autosampler); 3-88 min, 2-40% B; 88-98 min, 40-95% B; 98-99 min, 95% B; 99-100 min, 95-2% B; 100-110 min (column re-equilibration), 2% B. A Q Exactive Plus mass spectrometer (Thermo Scientific), equipped with a nanoelectrospray ionization source, was used to mass analyze the eluting peptides using a data-dependent method. The instrument method consisted of MS1 using an MS AGC target value of 3e6, followed by up to 20 MS/MS scans of the most abundant ions detected in the preceding MS scan. A maximum MS/MS ion time of 60 ms was used with a MS2 AGC target of 1e5. Dynamic exclusion was set to 15s, HCD collision energy was set to 28 nce, and peptide match and isotope exclusion were enabled. For identification of peptides, tandem mass spectra were searched with Sequest (Thermo Fisher Scientific) against a *Mus musculus* database created from the UniprotKB protein database (www.uniprot.org). Variable modification of +15.9949 on Met (oxidation) and +57.0214 on Cys (carbamidomethylation) were included for database searching. Search results were assembled using Scaffold 4.3.2. (Proteome Software).

MRM-MS: Peptides for each protein were selected based on their appearance in data dependent analyses and then optimized for the most useful transitions to monitor. Heavy-labeled peptide internal standards were synthesized by jpt (SpikeTides TQL peptides, jpt, Berlin, Germany) which contained isotopically-labeled terminal arginine or lysine residues (^{13}C and ^{15}N) and a trypsin-removable C-terminal tag. These isotopically-labeled peptides were digested separately and then spiked into samples at approximately endogenous levels after in-gel digestion of sample proteins. Skyline software (University of Washington, MacCoss lab) was used to set up scheduled, targeted MRM methods monitoring four to five MRM transitions per peptide. A final MRM instrument method including the isotopically labeled standards and encompassing a 9-minute window around the retention time of each peptides was performed using a 40 mm by 0.1 mm (Jupiter 5 micron, 300A) kasil fritted trap followed by a 250 mm by 0.1 mm (Jupiter 3 micron, 300A), self-packed analytical column coupled directly to an TSQ-Vantage (ThermoFisher) via a nanoelectrospray source. Peptides were resolved using an aqueous to organic gradient flowing at 400 nl/min. Q1 peak width resolution was set to 0.7, collision gas pressure was 1 mTorr, and utilized an EZmethod cycle time of 3 seconds.

Single molecule approach to assess protein-protein interactions

Surface cleaning: No. 1.5 glass coverslips (Electron Microscopy Sciences) and quartz slides were (Ted Pella Inc.) rinsed in 100% ethanol, followed by acetone and sonicated for 15 min. Coverslips and slides were then put in 1M KOH (Sigma-Aldrich) and sonicated for an additional 30 min, followed with 3 rinsed in ultrapure water, and additional rinses in acetone. The materials were further

cleaned in 0.5 vol-% Helmanex III solution for 30 minutes followed by rinsing in ultrapure water three times. Surfaces were then sonicated for 10 min in 99.9% HPLC-grade methanol (Fisher Chemical). The surfaces were finally torched by swiping three times over a Bunsen burner.

Labeling, cell lysis and imaging: Approximately 300,000 cells from 24-well plates were used. Cells were first labeled with JF585-Halo dye for 90 min, followed by extensive 5x washes with PBS to remove any unbound dye. Cells were then lysed in ice-cold lysis buffer (20mM Hepes, 50mM NaCl, 2mM EDTA, 0.15% Triton X-100), centrifuged at 13,000*xg* for 5 min to remove debris and a fraction of the cleared lysate was spread in between clean quartz slides and a glass coverslip for imaging. Images were taken using a Nikon TIRF microscope, Apo-TIRF 100x/1.49 oil immersion lens online with a Photometrics Prime 95B sCMOS camera. Both GFP and JF585-Halo were simulatenously excited using AOTF driven Nikon LUN-F multi-excitation diode laser lines firing 488nm and 561nm lasers and images collected on the camera using an Optosplit III setup (Cairn Research). Images were taken at 12.5Hz for 40 sec. Photobleaching steps were analyzed in Matlab using the algorithm described previously (Shivnaraine et al., 2016). Fraction bound was determined according to colocalization of green and red particles, analyzed in FIJI.

Determining HaloTag labeling efficiency: To determine the efficiency of HaloTag labeling in NMuMG cells we created a Venus-HaloTag fusion construct in lentiviral vector pLV-Venus. HaloTag coding sequence was inserted C-terminally to Venus between restriction sites BamHI/NdeI. Venus-Halo was expressed in NMuMG cells to test HaloTag labeling efficiency on incubation for 1.5h with different concentration of JF585-labeled-HaloTag ligand, or incubating cells with a single concentration of the ligands for 1h or 18h. Labeling efficiency was determined by spreading the cleared cell lysates as described above and calculated according to the expression:

$$\text{Labeling Efficiency} = \frac{Halo}{(Venus \cup Halo)}$$

Live cell TIRFM imaging and analysis

TIRF images were collected with an Andor Zyla sCMOS on Nikon Ti-E or a Photometrics Prime 95B mounted on a Nikon Ti-2 microscope, using an Apo TIRF 60x/1.49 oil immersion lens. The Nikon Ti-E TIRF microscope was equipped with multi-excitation diode laser lines (405nm,488nm, 561nm and 647nm) with triggering capabilities for fast dual color acquisitions, as described above.

Image acquisitions were performed using NIS Elements Advanced Research imaging software [version 4.60.00 (Build 1171) Patch 02]. Images were processed and analyzed with Elements or FIJI.

For analysis of single fusion events, each acquired image sequence was manually reviewed multiple times to visually identify vesicle fusion events as demarcated by Vamp2-pHluorin or TfR-pHuji fluorescence intensity flashes. Coordinates of the vesicle fusion events were marked by a circular ROI. GFP or mApple particle durations were analyzed using NIS-Elements. Circular ROIs ~1 μm were drawn inside the initial ROIs and were used to calculate the intensities of sfGFP and pHuji. Arrival and departure of sfGFP were determined based on their increase and decrease in intensities, respectively. Kymographs of sfGFP and pHuji were generated and analyzed using NIS-Elements.

Photobleaching step detection in Figure 4 and Figure S4, was done in MATLAB using an algorithm described previously (Shivnaraine et al., 2016). Exocyst molecule numbers were estimated from GFP intensity standards. One, 2 or 3 sfGFP were fused to the C-terminus of monomeric CD86 and expressed in HEK293T cells (James et al., 2006). Intensities were measured at a fixed optimal camera and laser setting. Intensities of the molecules were matched to photobleaching steps and fitted to a linear regression model. The same instruments settings and the region of the image with uniform intensities were then used to measure exocyst molecule intensities during vesicle fusions. The peak intensities of single resolved sfGFP-exocyst particles at vesicle fusion sites, indicated by TfR-pHuji, were then measured and the number of molecules/particle determined from the regression equation. Figure S5E-I further explains the criterions used for fluorescence intensity measurements.

Mean squared displacements of the different exocyst subunits from TIRFM images were measured using Imaris image analysis software (Bitplane) tracking algorithm. For two-color tracking, each channel was individually processed and overlaid to assess differences in overall diffusion patterns.

Dual Color Fluorescence Cross-Correlation Spectroscopy in Live Cells

Experimental setup - dcFCS measurements were performed on a custom-built instrument using a hardware correlator (Zhang et al., 2017). The system is a confocal microscope built with multicolor excitation and detection and with real-time multi-channel correlation analysis capabilities. sfGFP and JF646 were excited simultaneously by a blue laser (TECBL-488nm, WorldStarTech) and a red laser (TECRL-633nm, WorldStarTech). Excitation power at the sample was set in the range of 0.1 – 5 μW, corresponding to an average intensity of 0.05 – 2.5 kW/cm^2 in the diffraction-limited confocal area. Fluorescence signals from sfGFP and JF646 were separated by a dichroic filter (FF585-Di01,

Semrock) and directed through a green bandpass filter (FF01-512/25, Semrock) in the case of eGFP or a red longpass filter (LP02-647RS, Semrock) in the case of JF646. Each signal was split using a 50/50 non-polarizing beamsplitter. The four signals were collected using four avalanche photodiode (APD) detectors (SPCM-AQR-13-FC, PerkinElmer Inc.) and processed by a multichannel hardware correlator (Flex11-8Ch, correlator.com). The correlator outputs up to four different intensity correlation curves between any two detection channels. For typical live cell measurements, at least 10^7 photons were collected from each cell to construct the FCS curves.

Live cell measurements – Experiments on NMuMG cells were performed using glass-bottomed Petri-dishes (MatTek), in which the cells grow on a round coverslip located in the center at the bottom of the dish. All imaging was performed in FluoroBrite DMEM media (Thermo Fisher Scientific). Confocal scan imaging was employed to search for cells that exhibit an optimal fluorescence signal of 5 - 100 kHz at a laser excitation intensity of 50 - 250 W/cm^2. The software-controlled raster scan was performed using a piezo nano-positioning stage (Nano-LP100, Mad City Labs Inc.), which has a 100-μm scanning range on each of the three axes. There typically was less than one cell suitable for FCS measurements within the 100- μm field of view. A mechanical translation stage was used to bring new 100-μm regions of the dish into the field of view of the microscope. This allowed for the survey of multiple cells in multiple regions within a single dish, thus improving efficiency of data collection and the statistical reliability of data analysis.

Model-fitting for FCS

Correlation curves from dcFCS were analyzed in MATLAB using a custom-written program based on the Marquardt-Levenburg algorithm. The data were weighted according to the standard deviation at each point, as determined from multiple repeated readings. Rhodamine 110 and Alexa Fluor 647 were measured in an aqueous PBS buffer to calibrate geometrical parameters (lateral radius, w_0, and aspect ratio, s) of the confocal detection volumes, which were approximated as 3D Gaussians.

For exocyst proteins diffusing in live cells, a 2-component diffusion model was applied to fit the three correlation curves, namely green auto-correlation (for GFP), red auto-correlation (for JF-646), and cross-correlation:

$$\begin{aligned} G_{\mathrm{j}}(\tau) &= G_{\mathrm{j}}(0)\left(f_{\mathrm{D1}} \cdot Diff_{\mathrm{D1,j}}(\tau) + f_{\mathrm{D2}} \cdot Diff_{\mathrm{D2}}(\tau)\right),\ \mathrm{j} = \mathrm{g}\ or\ \mathrm{r} \\ G_{\mathrm{x}}(\tau) &= G_{\mathrm{x}}(0) \cdot Diff_{D2}(\tau) \end{aligned} \tag{1}$$

where the diffusion terms are expressed as:

$$Diff_{\mathrm{D1,j}} = \left(1+\frac{\tau}{\tau_{\mathrm{D1,j}}}\right)^{-1}\left(1+\frac{1}{s^2}\cdot\frac{\tau}{\tau_{\mathrm{D1,j}}}\right)^{-1/2}, \ \mathrm{j = green}\ or\ \mathrm{red};$$

$$Diff_{\mathrm{D2}} = \left(1+\frac{\tau}{\tau_{\mathrm{D2}}}\right)^{-1}\left(1+\frac{1}{s^2}\cdot\frac{\tau}{\tau_{\mathrm{D2}}}\right)^{-1/2} \qquad \text{(2-a)}$$

for 3-dimensional diffusion in the cytosol, or:

$$Diff_{\mathrm{D1,j}} = \left(1+\frac{\tau}{\tau_{\mathrm{D1,j}}}\right)^{-1}, \ \mathrm{j = green}\ or\ \mathrm{red};$$

$$Diff_{\mathrm{D2}} = \left(1+\frac{\tau}{\tau_{\mathrm{D2}}}\right)^{-1} \qquad \text{(2-b)}$$

for 2-dimensional diffusion at the membrane.

Note that the cross-correlation contains only one diffusion component, which has the same parameters as the slow diffusion component of the green and the red auto-correlation curves. In Eqs. 2, τ_{D1} and τ_{D2} are the residence times of the two diffusing species, and f_{D1} and f_{D2} are corresponding fluorescence intensity contributions of the two diffusion species ($f_{D1} + f_{D2} = 1$). In the case of monomeric proteins, f_{D1} and f_{D2} equal to the concentration fractions of the two diffusing species. Diffusion coefficients (D) were calculated from fitted estimate of τ_D values as $D = w_0^2/4\tau_D$, where w_0 is the lateral radius of the detection volume.

Fractions of coupling are then calculated from the correlation amplitudes after fitting to Eqs. 1(Bacia and Schwille, 2007):

$$\text{fraction of green} = \frac{G_x(0)}{G_r(0)}$$

$$\text{fraction of red} = \frac{G_x(0)}{G_g(0)} \qquad \text{(3)}$$

Fractions of coupling calculated from Eqs. 3 were corrected for spectral cross-talk using available fluorescence intensity information (Bacia et al., 2012). Correction factors were consistently lower than 0.1% owing to the high fluorescence intensity of the JF-646 dye relative to GFP. In addition, the fractions were not corrected for possible detection volume misoverlap due to the lack of a reliable in-cell control sample. This may lead to an underestimation by a constant scaling factor, which does not affect the comparison of measured fractions of coupling across different cells/samples.

Statistical Analysis

Data are reported as ± s.d., ± s.e.m or 25th-75th IQR, and analyzed by Student's *t*-test or one-way analysis of variance (ANOVA) as indicated using Graphpad Prism 7, R, or JASP (ver.0.8.6) statistical softwares. For curve fitting, fits were assessed by accounting for variation in the FCS data curve and Chi-square test statistics. When using ANOVA or Kruskal-Wallis test, *post hoc* analysis was done using Tukey's, Dunn's or Scheffe's multiple comparison tests as appropriate. All statistical analysis was considered significant at $p < 0.05$.

Figure 1

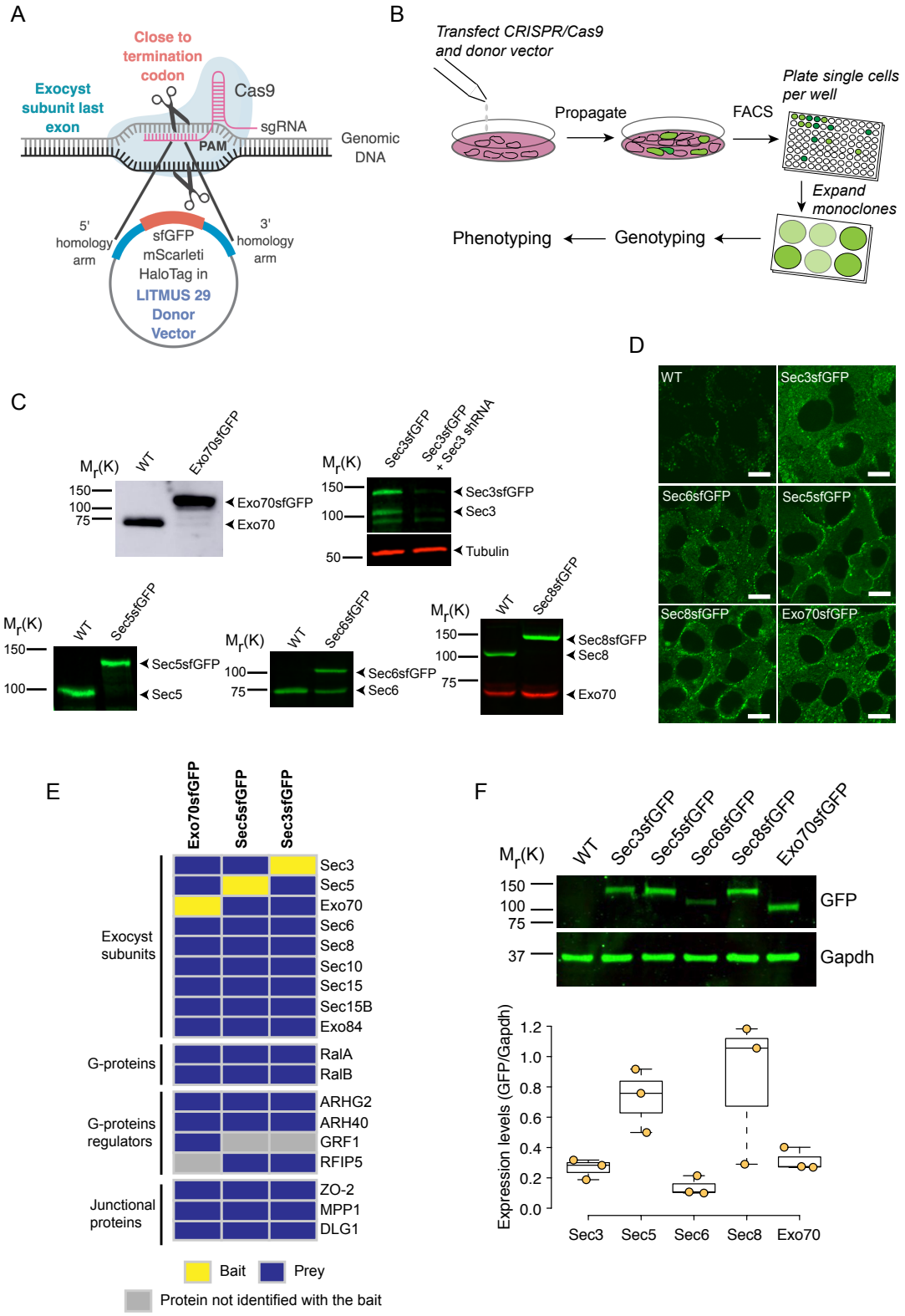
A
Close to termination codon
Exocyst subunit last exon
Cas9
sgRNA
PAM
Genomic DNA
5' homology arm
3' homology arm
sfGFP
mScarleti
HaloTag in
LITMUS 29
Donor
Vector
B
Transfect CRISPR/Cas9 and donor vector
Propagate
FACS
Plate single cells per well
Expand monoclones
Genotyping
Phenotyping
C
Mr(K)
WT
Exo70sfGFP
Exo70sfGFP
Exo70
Sec3sfGFP
Sec3sfGFP + Sec3 shRNA
Sec3sfGFP
Sec3
Tubulin
Sec5sfGFP
Sec5
Sec6sfGFP
Sec6
Sec8sfGFP
Sec8
Exo70
D
WT
Sec3sfGFP
Sec6sfGFP
Sec5sfGFP
Sec8sfGFP
Exo70sfGFP
E
Exo70sfGFP
Sec5sfGFP
Sec3sfGFP
Exocyst subunits
Sec3
Sec5
Exo70
Sec6
Sec8
Sec10
Sec15
Sec15B
Exo84
G-proteins
RalA
RalB
G-proteins regulators
ARHG2
ARH40
GRF1
RFIP5
Junctional proteins
ZO-2
MPP1
DLG1
Bait
Prey
Protein not identified with the bait
F
Mr(K)
WT
Sec3sfGFP
Sec5sfGFP
Sec6sfGFP
Sec8sfGFP
Exo70sfGFP
GFP
Gapdh
Expression levels (GFP/Gapdh)
Sec3
Sec5
Sec6
Sec8
Exo70

Figure 2

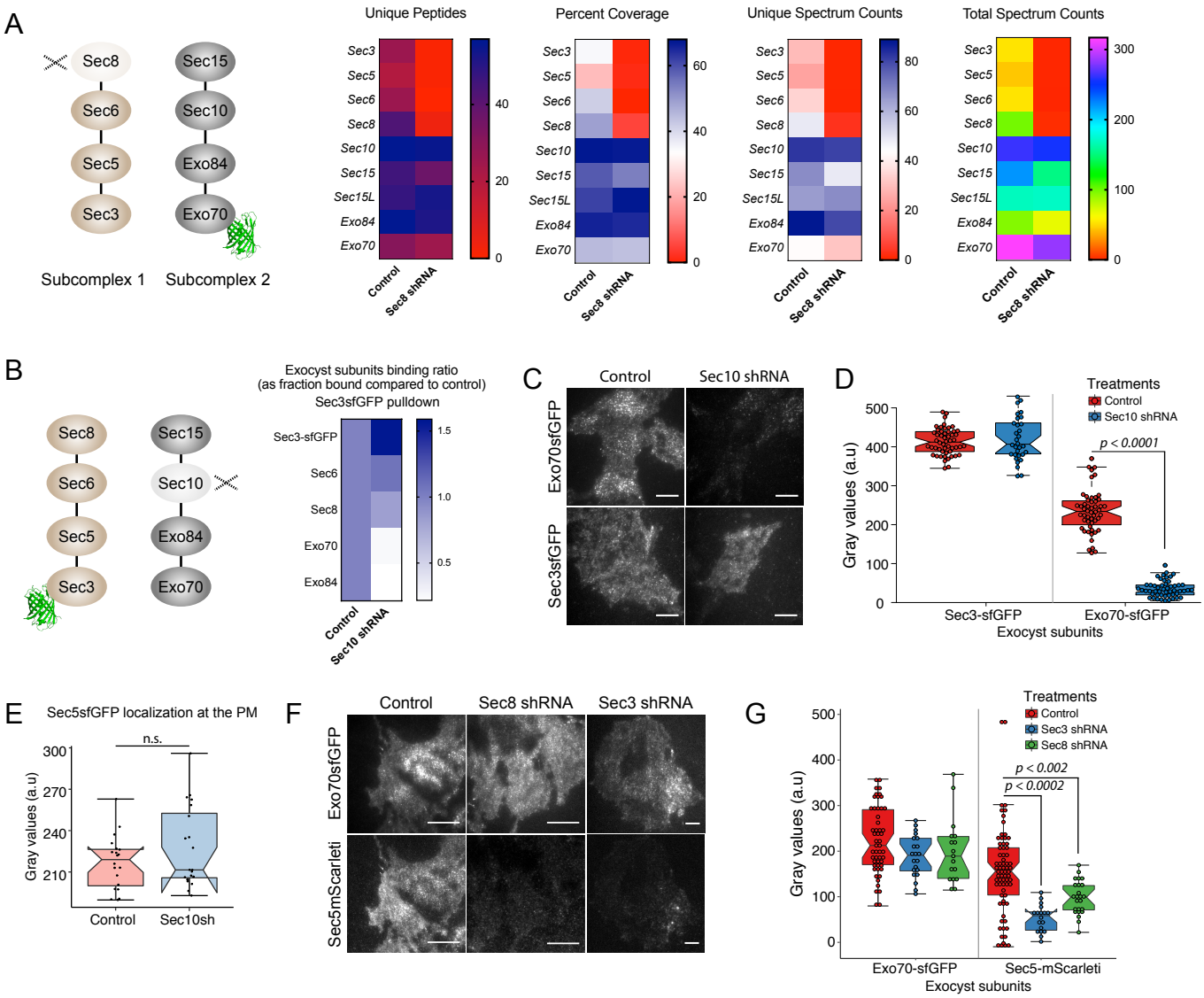
A
Sec8
Sec6
Sec5
Sec3
Sec15
Sec10
Exo84
Exo70
Subcomplex 1
Subcomplex 2
Unique Peptides
Percent Coverage
Unique Spectrum Counts
Total Spectrum Counts
Sec3
Sec5
Sec6
Sec8
Sec10
Sec15
Sec15L
Exo84
Exo70
Control
Sec8 shRNA
B
Exocyst subunits binding ratio
(as fraction bound compared to control)
Sec3sfGFP pulldown
Sec3-sfGFP
Sec10 shRNA
C
Control
Sec10 shRNA
Exo70sfGFP
Sec3sfGFP
D
Treatments
Control
Sec10 shRNA
p < 0.0001
Gray values (a.u)
Sec3-sfGFP
Exo70-sfGFP
Exocyst subunits
E
Sec5sfGFP localization at the PM
n.s.
Gray values (a.u)
Control
Sec10sh
F
Control
Sec8 shRNA
Sec3 shRNA
Exo70sfGFP
Sec5mScarleti
G
Treatments
Control
Sec3 shRNA
Sec8 shRNA
p < 0.002
p < 0.0002
Gray values (a.u)
Exo70-sfGFP
Sec5-mScarleti
Exocyst subunits

Figure 3

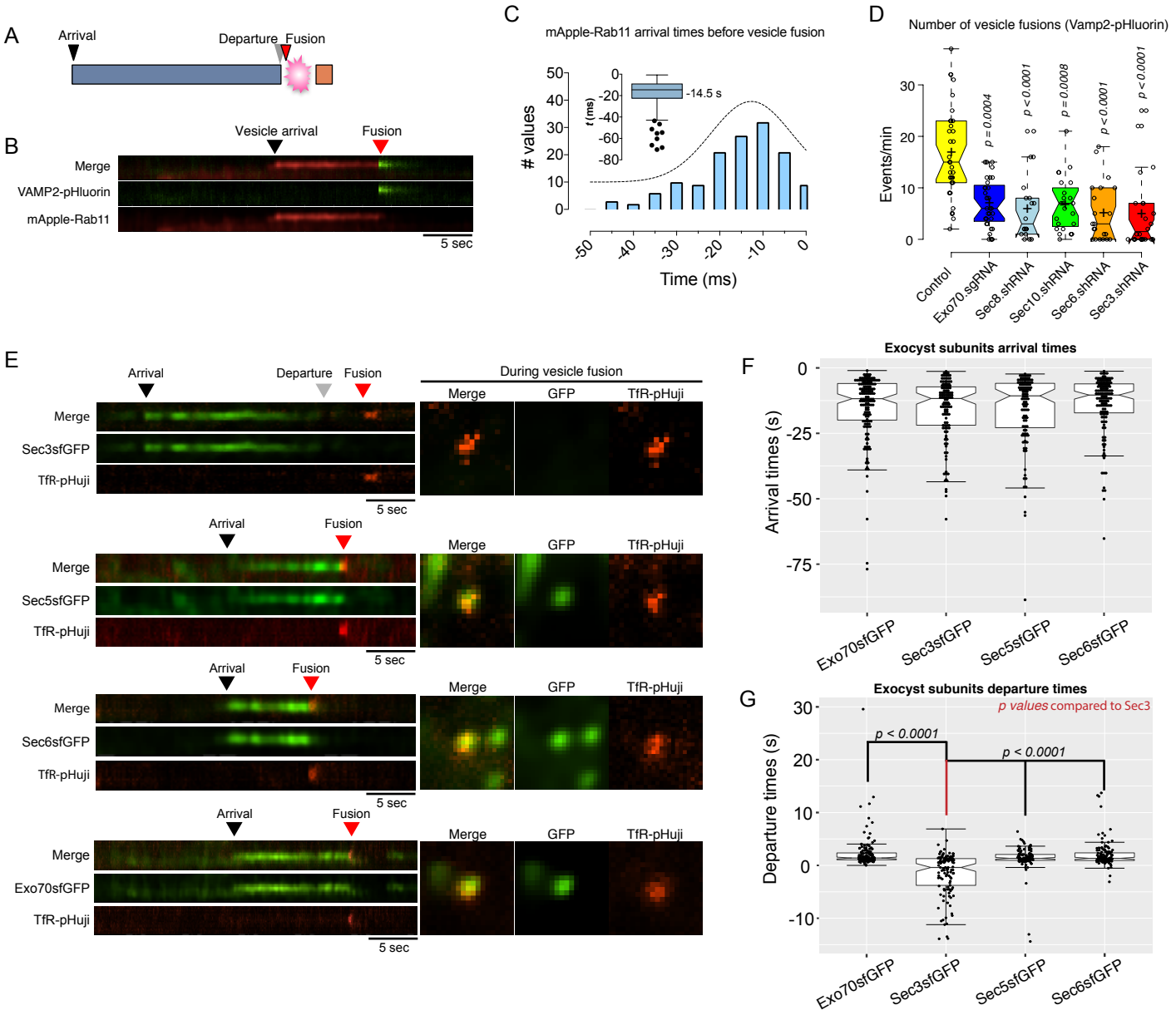
A
Arrival
Departure
Fusion
B
Vesicle arrival
Fusion
Merge
VAMP2-pHluorin
mApple-Rab11
5 sec
C
mApple-Rab11 arrival times before vesicle fusion
values
t (ms)
-14.5 s
Time (ms)
D
Number of vesicle fusions (Vamp2-pHluorin)
Events/min
p = 0.0004
p < 0.0001
p = 0.0008
p < 0.0001
p < 0.0001
Control
Exo70.sgRNA
Sec8.shRNA
Sec10.shRNA
Sec6.shRNA
Sec3.shRNA
E
Arrival
Departure
Fusion
During vesicle fusion
Merge
GFP
TfR-pHuji
Sec3sfGFP
Sec5sfGFP
Sec6sfGFP
Exo70sfGFP
F
Exocyst subunits arrival times
Arrival times (s)
Exo70sfGFP
Sec3sfGFP
Sec5sfGFP
Sec6sfGFP
G
Exocyst subunits departure times
p values compared to Sec3
p < 0.0001
p < 0.0001
Departure times (s)

Figure 4

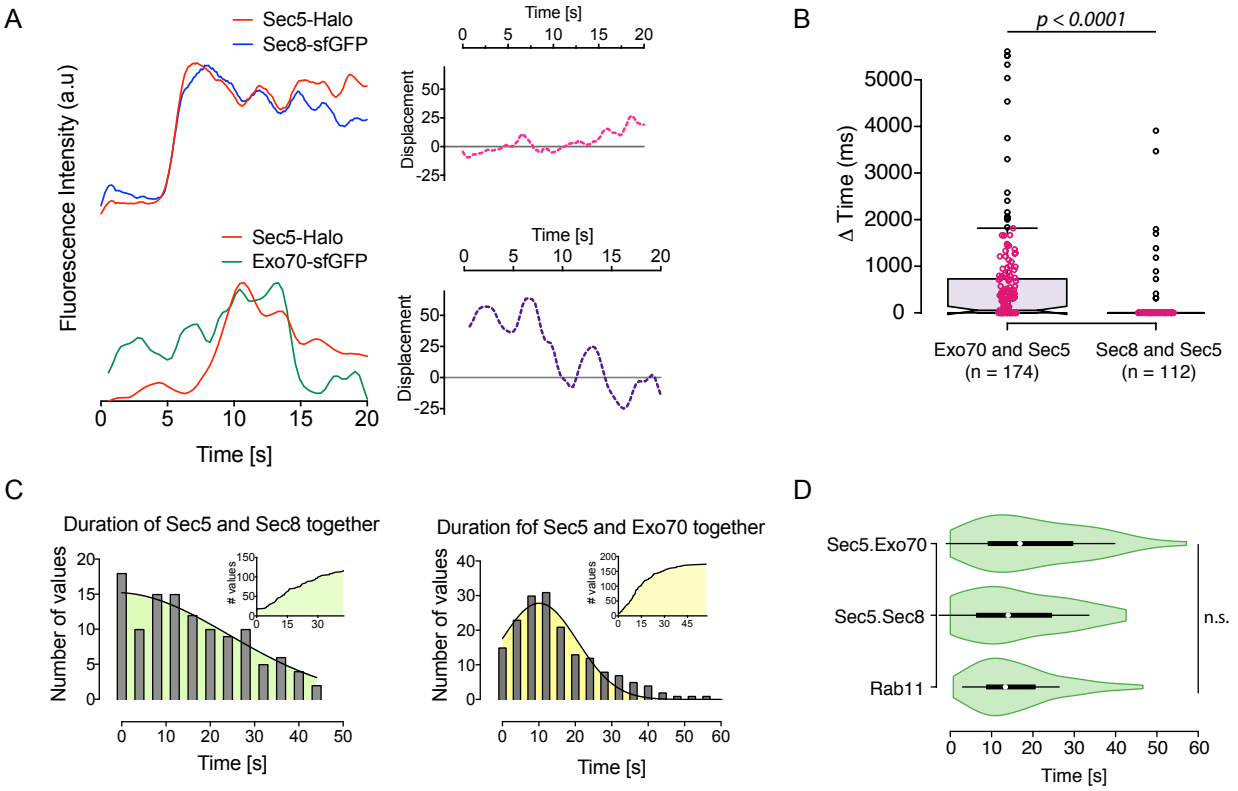
A
Sec5-Halo
Sec8-sfGFP
Fluorescence Intensity (a.u)
Time [s]
Displacement
Sec5-Halo
Exo70-sfGFP
B
p < 0.0001
Δ Time (ms)
Exo70 and Sec5
(n = 174)
Sec8 and Sec5
(n = 112)
C
Duration of Sec5 and Sec8 together
Number of values
values
Time [s]
Duration fof Sec5 and Exo70 together
D
Sec5.Exo70
Sec5.Sec8
Rab11
n.s.

Figure 5

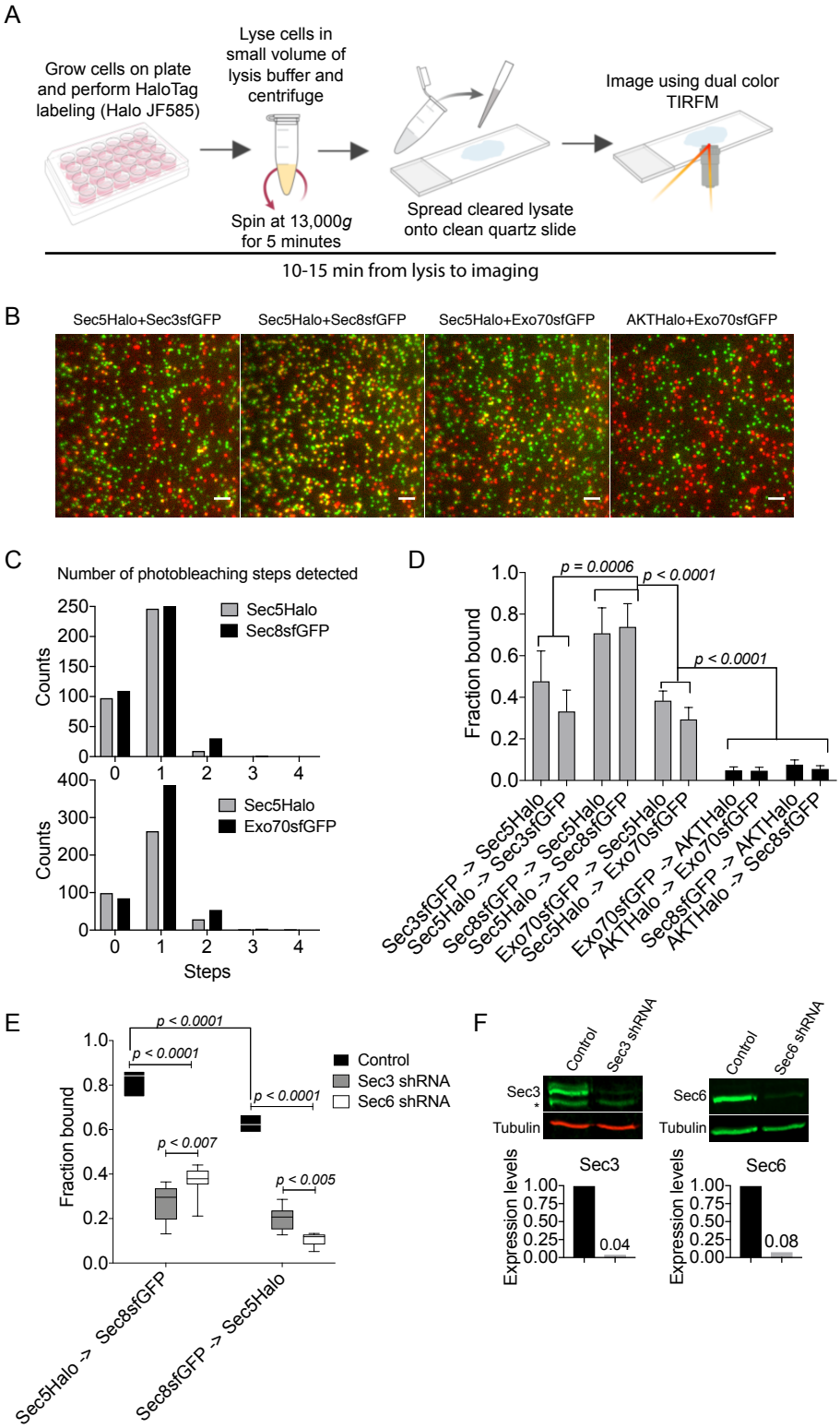
A
Grow cells on plate and perform HaloTag labeling (Halo JF585)
Lyse cells in small volume of lysis buffer and centrifuge
Spin at 13,000g for 5 minutes
Spread cleared lysate onto clean quartz slide
Image using dual color TIRFM
10-15 min from lysis to imaging
B
Sec5Halo+Sec3sfGFP
Sec5Halo+Sec8sfGFP
Sec5Halo+Exo70sfGFP
AKTHalo+Exo70sfGFP
C
Number of photobleaching steps detected
Sec5Halo
Sec8sfGFP
Exo70sfGFP
Counts
Steps
D
Fraction bound
p = 0.0006
p < 0.0001
Sec3sfGFP -> Sec5Halo
Sec5Halo -> Sec3sfGFP
Sec8sfGFP -> Sec5Halo
Sec5Halo -> Sec8sfGFP
Exo70sfGFP -> Sec5Halo
Sec5Halo -> Exo70sfGFP
AKTHalo -> Exo70sfGFP
Exo70sfGFP -> AKTHalo
AKTHalo -> Sec8sfGFP
Sec8sfGFP -> AKTHalo
E
Control
Sec3 shRNA
Sec6 shRNA
p < 0.007
p < 0.005
Sec5Halo -> Sec8sfGFP
Sec8sfGFP -> Sec5Halo
F
Control
Sec3 shRNA
Sec6 shRNA
Sec3
Sec6
Tubulin
Expression levels
0.04
0.08

Figure 6

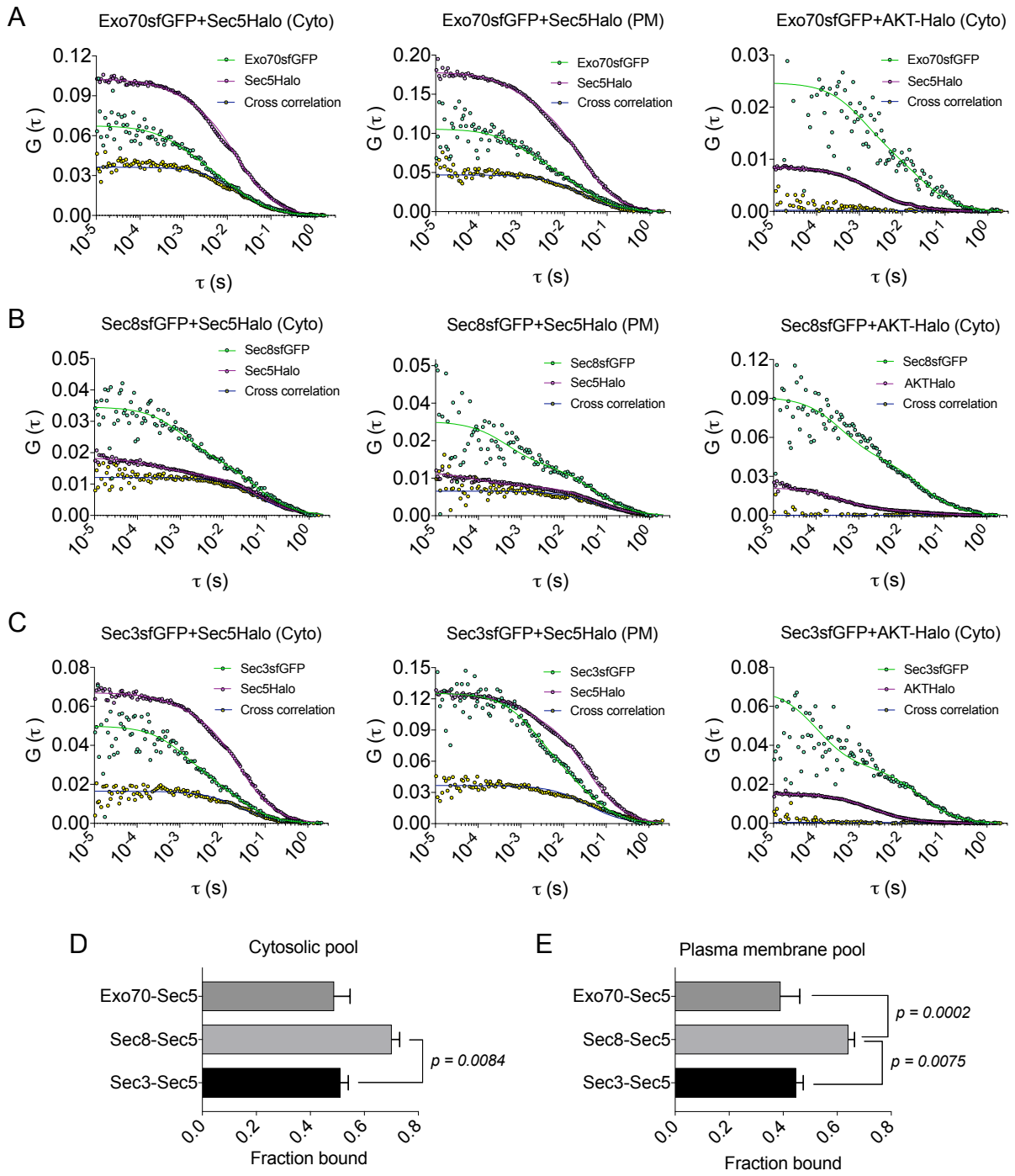
A
Exo70sfGFP+Sec5Halo (Cyto)
Exo70sfGFP+Sec5Halo (PM)
Exo70sfGFP+AKT-Halo (Cyto)
Exo70sfGFP
Sec5Halo
Cross correlation
G (τ)
τ (s)
B
Sec8sfGFP+Sec5Halo (Cyto)
Sec8sfGFP+Sec5Halo (PM)
Sec8sfGFP+AKT-Halo (Cyto)
Sec8sfGFP
Sec5Halo
AKTHalo
Cross correlation
C
Sec3sfGFP+Sec5Halo (Cyto)
Sec3sfGFP+Sec5Halo (PM)
Sec3sfGFP+AKT-Halo (Cyto)
Sec3sfGFP
Sec5Halo
AKTHalo
Cross correlation
D
Cytosolic pool
Exo70-Sec5
Sec8-Sec5
Sec3-Sec5
p = 0.0084
Fraction bound
E
Plasma membrane pool
Exo70-Sec5
Sec8-Sec5
Sec3-Sec5
p = 0.0002
p = 0.0075
Fraction bound

Figure 7

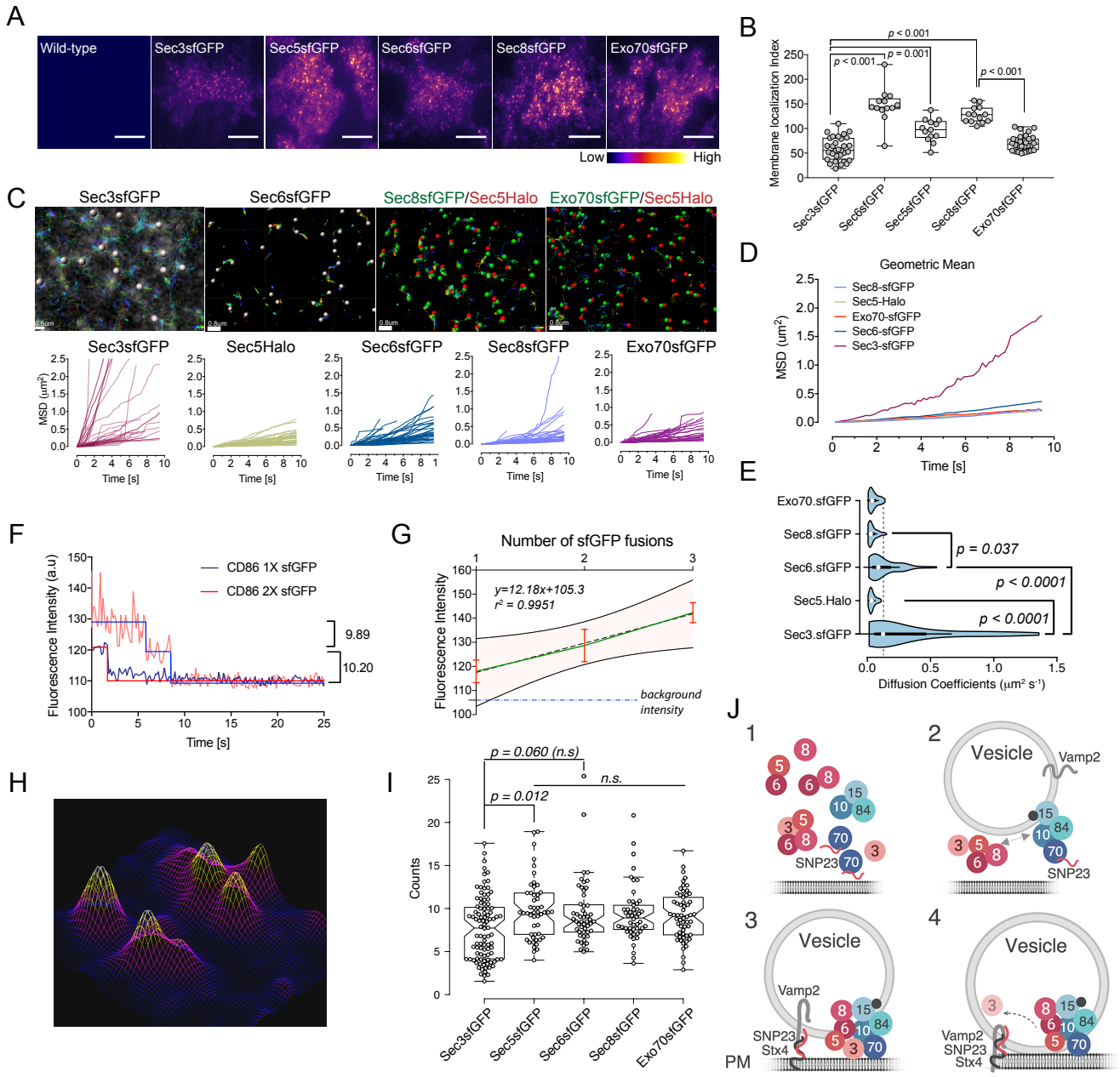
A
Wild-type
Sec3sfGFP
Sec5sfGFP
Sec6sfGFP
Sec8sfGFP
Exo70sfGFP
Low
High
B
Membrane localization Index
p < 0.001
p = 0.001
Sec3sfGFP
Sec6sfGFP
Sec5sfGFP
Sec8sfGFP
Exo70sfGFP
C
Sec3sfGFP
Sec6sfGFP
Sec8sfGFP/Sec5Halo
Exo70sfGFP/Sec5Halo
Sec5Halo
MSD (μm²)
Time [s]
D
Geometric Mean
Sec8-sfGFP
Sec5-Halo
Exo70-sfGFP
Sec6-sfGFP
Sec3-sfGFP
E
Exo70.sfGFP
Sec8.sfGFP
Sec6.sfGFP
Sec5.Halo
Sec3.sfGFP
p = 0.037
p < 0.0001
Diffusion Coefficients (μm² s⁻¹)
F
Fluorescence Intensity (a.u)
CD86 1X sfGFP
CD86 2X sfGFP
9.89
10.20
G
Number of sfGFP fusions
y=12.18x+105.3
r² = 0.9951
Fluorescence Intensity
background intensity
H
I
p = 0.060 (n.s)
n.s.
p = 0.012
Counts
J
Vesicle
Vamp2
SNP23
Stx4
PM

Table 1. LC-MS/MS analysis of exocyst subunits interactions

			Unique peptides			Unique Spectra			Total Spectra			% Coverage		
			Exo70-sfGFP	Sec3-sfGFP	Sec5-sfGFP	Exo70-sfGFP	Sec3-sfGFP	Sec5-sfGFP	Exo70-sfGFP	Sec3-sfGFP	Sec5-sfGFP	Exo70-sfGFP	Sec3-sfGFP	Sec5-sfGFP
Accession #	**Protein Name**	**Mol wt**												
A6H5Z3	Exocyst complex component 6B (EXC6B), Sec15L	94 kDa	52	47	48	83	68	69	178	163	116	76	67	68
GFP	Green fluorescent protein	27 kDa	6	7	7	9	12	13	46	35	23	32	34	34
O35250	Exocyst complex component 7 (Exoc7), Exo70	80 kDa	**47**	43	45	**91**	68	71	**239**	167	128	**68**	65	67
O35382	Exocyst complex component 4 (Exoc4), Sec8	111 kDa	53	67	63	93	126	128	237	452	391	72	81	77
Q9D4H1	Exocyst complex component 2 (Exoc2), Sec5	104 kDa	45	57	**54**	65	97	**99**	162	396	**377**	61	68	**69**
Q6KAR6	Exocyst complex component 3 (Exoc3), Sec6	86 kDa	38	52	50	64	88	95	145	472	274	61	68	69
Q8R3S6	Exocyst complex component 1 (Exoc1), Sec3	102 kDa	40	**51**	49	72	**96**	105	145	**372**	268	59	**72**	68
Q3TPX4	Exocyst complex component 5 (Exoc5), Sec10	82 kDa	39	36	35	71	56	55	192	144	94	62	65	63
Q8R313	Exocyst complex component 6 (Exoc6), Sec15	93 kDa	36	30	32	62	42	41	146	95	73	62	53	56
Q6PGF7	Exocyst complex component 8 (Exoc8), Exo84	81 kDa	31	24	27	44	27	27	77	55	49	55	41	45
P63321	RALA	24 kDa	4	4	4	5	4	6	6	5	7	50	40	50
Q9JIW9	RALB	23 kDa	9	6	9	12	6	13	14	7	19	47	33	48
Q8R361	Rab11 family-interacting protein 5 (RFIP5)	70 kDa	5	0	3	5	0	3	5	0	3	10	0	6.2
Q3UPH7	Rho guanine nucleotide exchange factor 40 (ARH40)	165 kDa	7	14	7	7	14	7	7	16	7	5.5	12	5.6
Q91YM2	Rho GTPase-activating protein 35	170 kDa	0	6	0	0	6	0	0	6	0	0	6.3	0
Q60875	Rho guanine nucleotide exchange factor 2(ARHG2)	112 kDa	1	2	0	1	2	0	1	2	0	2	2.2	0
Q9Z0U1	Tight junction protein ZO-2	131 kDa	2	18	13	2	18	13	2	25	14	2.1	17	13
Q811D0	Disks large homolog 1 (Dlg1)	100 kDa	12	26	25	12	30	27	14	48	36	20	44	42
O09044	Synaptosomal-associated protein 23 (SNAP23)	23 kDa	6	-	-	6	-	-	6	-	-	39	-	-
Q8BVD5	MAGUK p55 subfamily member 7 (MPP7)	66 kDa	1	6	8	1	6	8	1	7	9	2.1	15	18

Mass spectrometry analysis of tryptic peptides fragments upon GFP-TRAP pull-down of Exo70-sfGFP, Sec3-sfGFP and Sec5-sfGFP from CRISPR knockin NMuMg cell lines. Only peptides determined with > 99%, and protein determined with >95% probability are shown.

Supplementary Figure 1

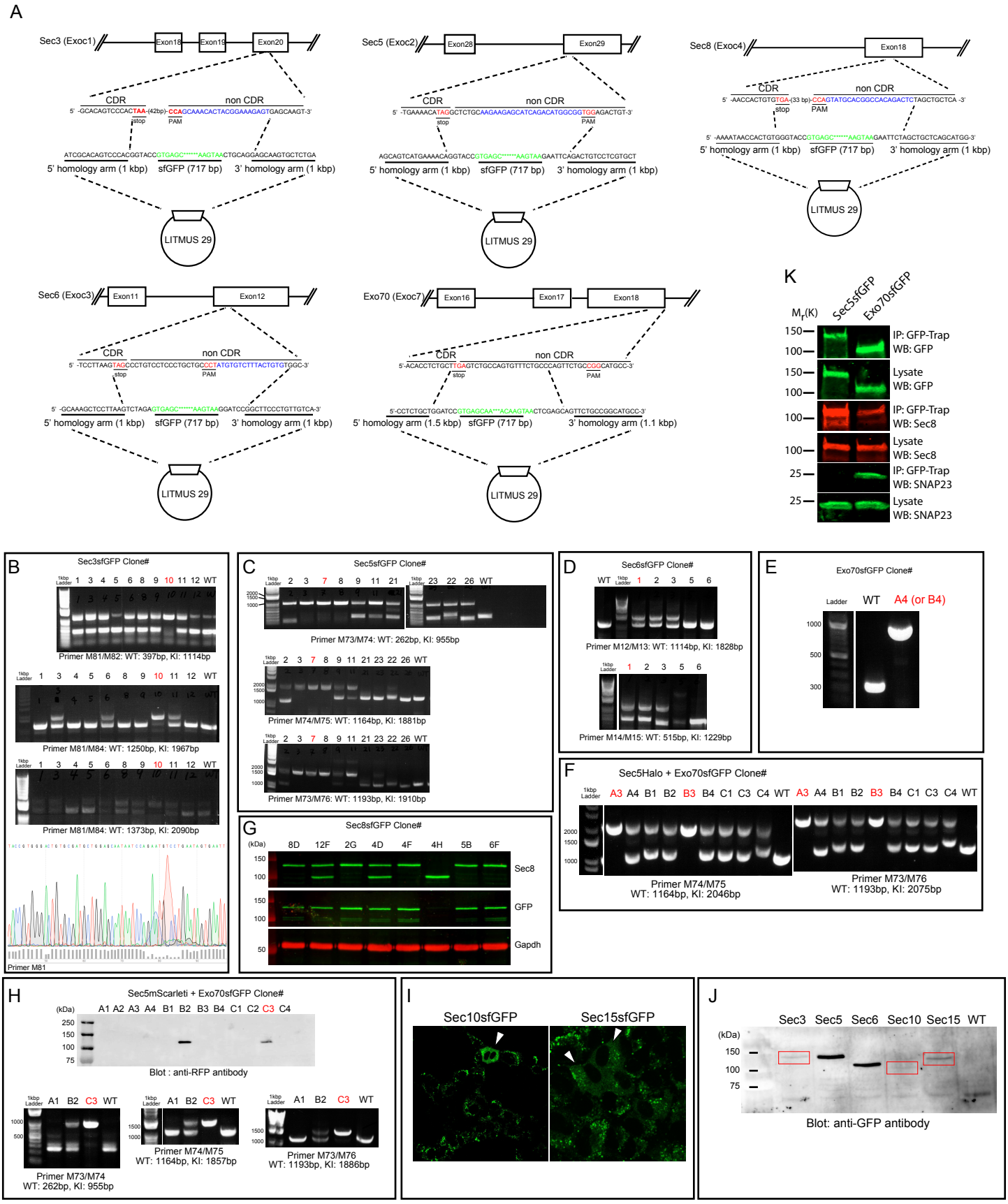

Supplementary Figure 2

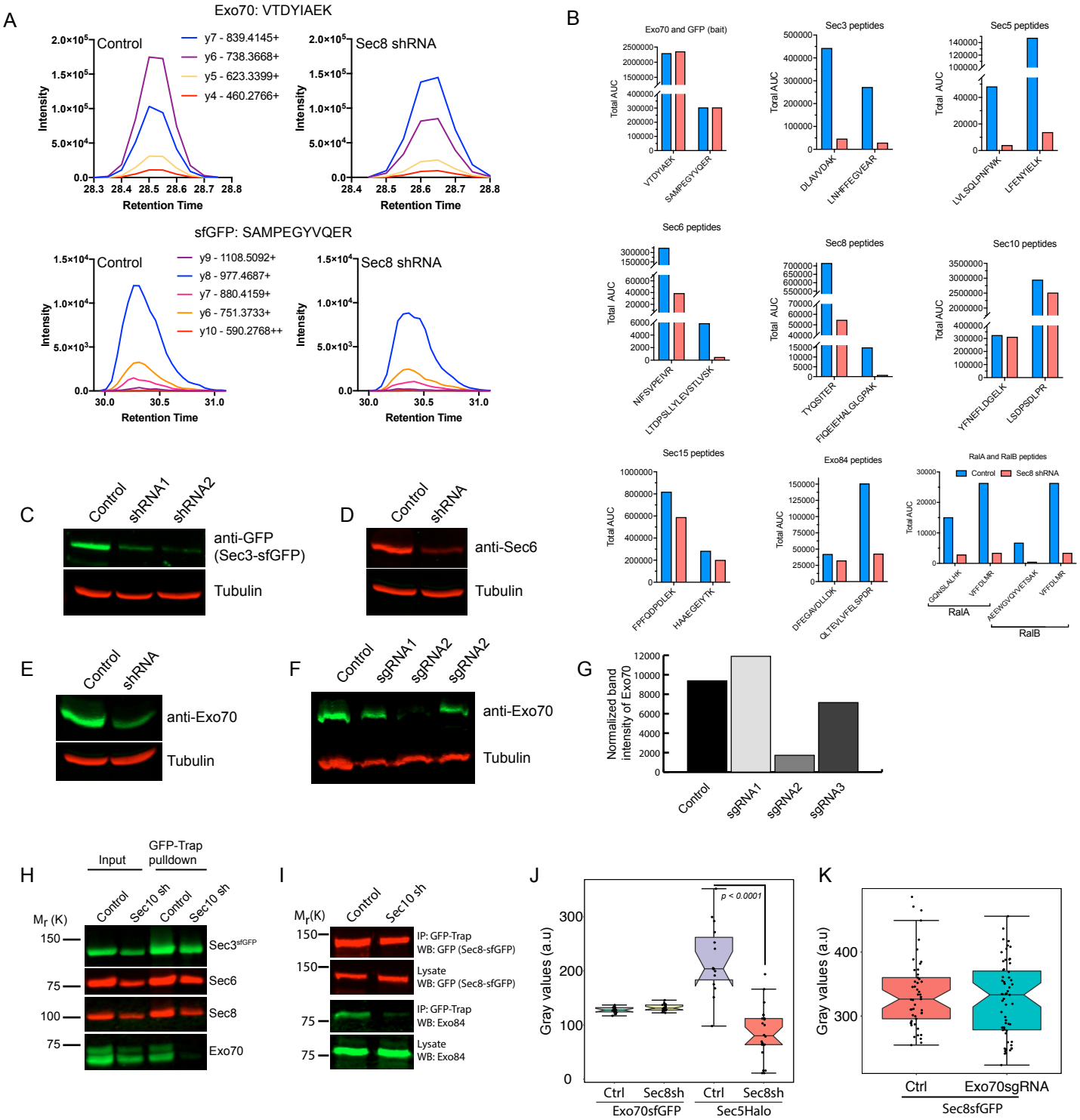

Supplementary Figure 3

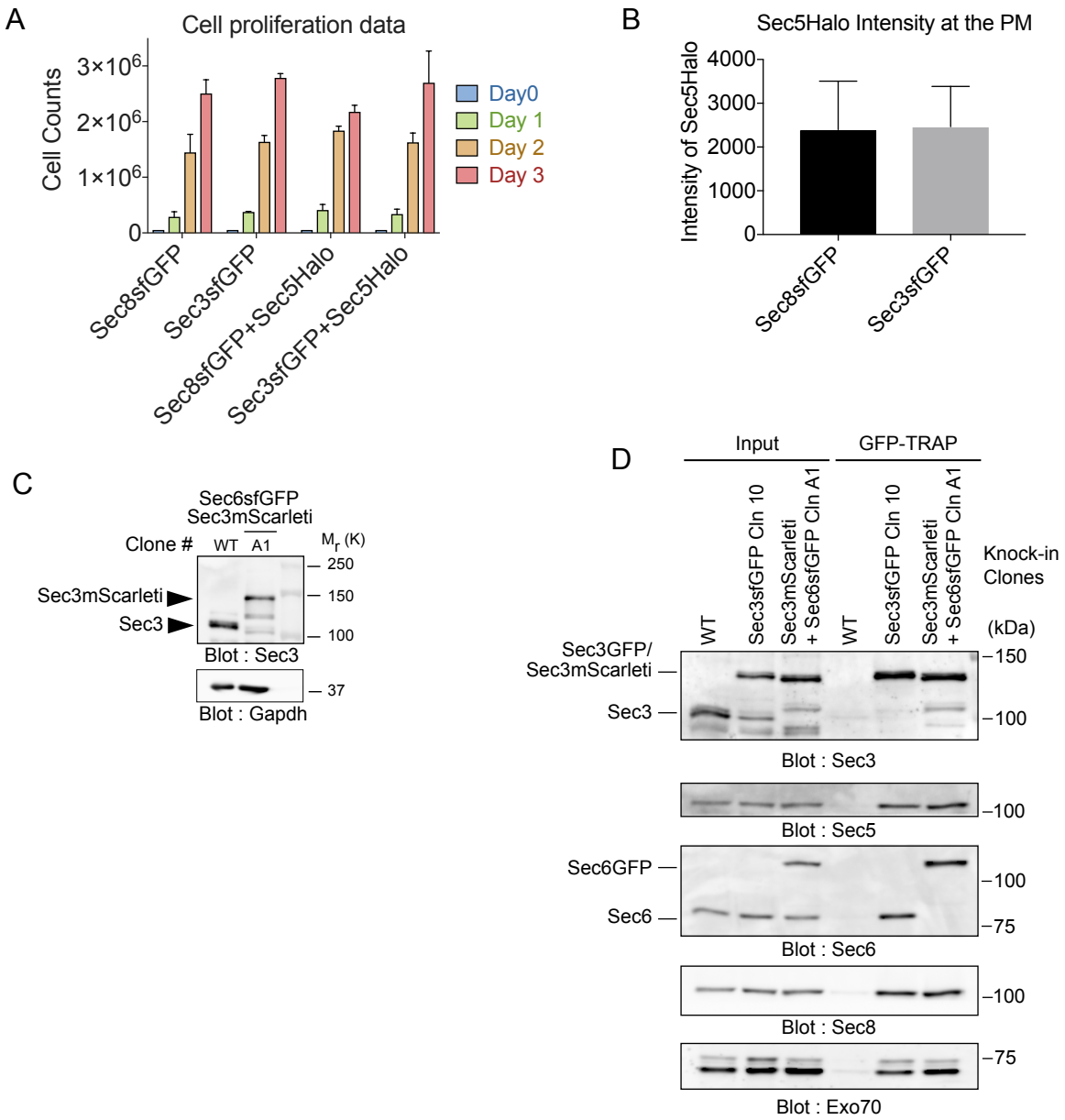

Supplementary Figure 4

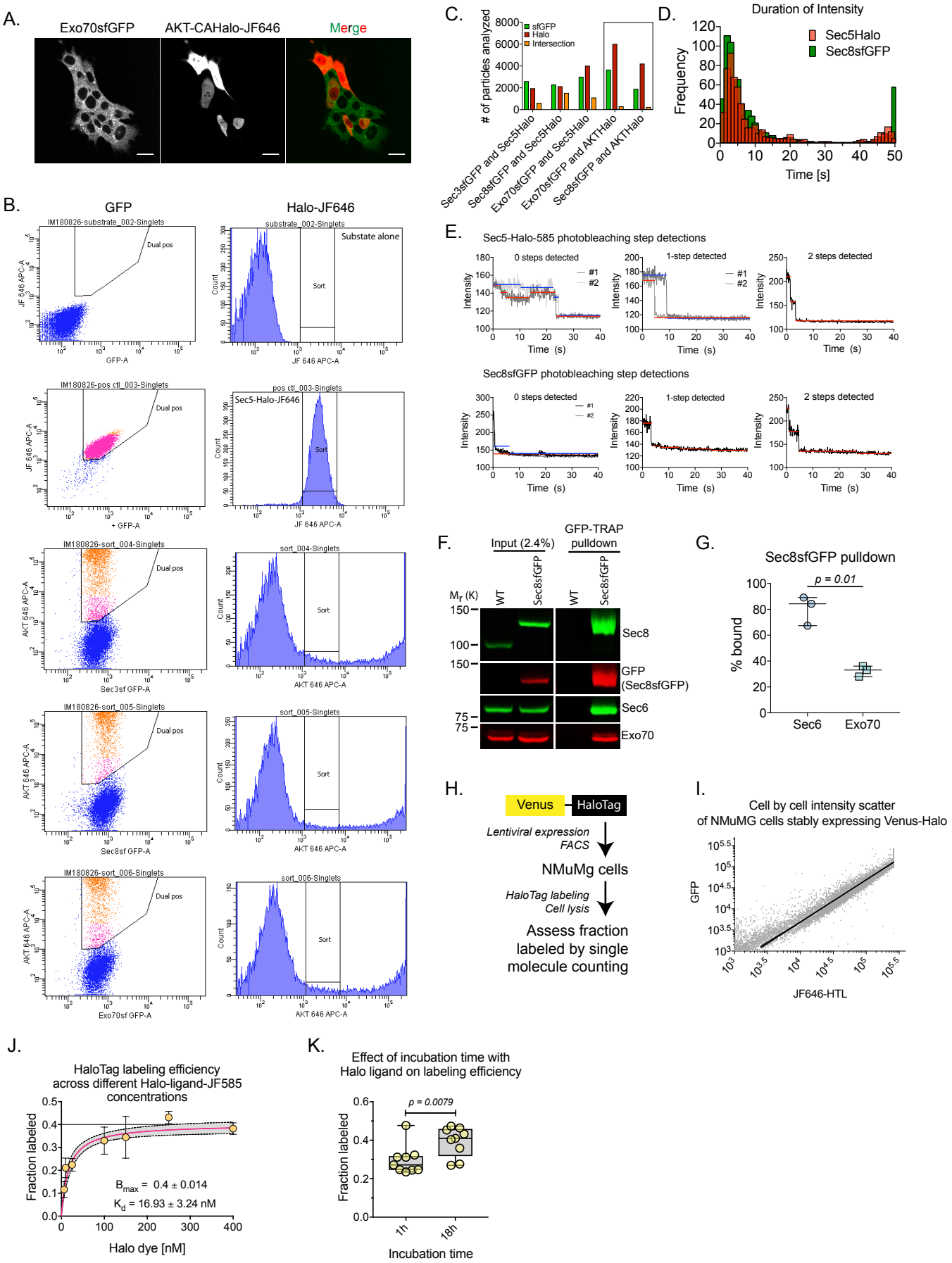
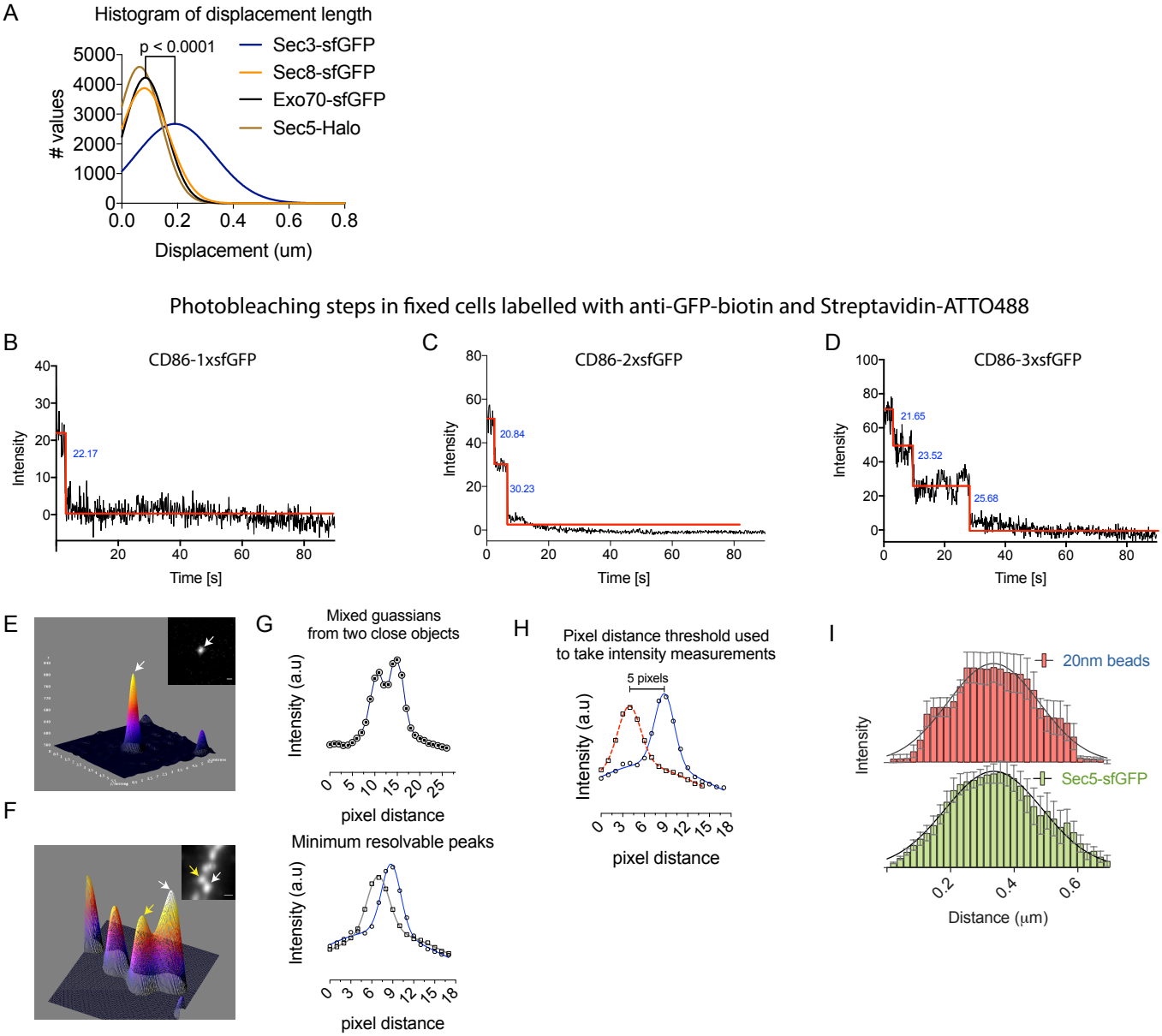
Supplementary Figure 5